

Lattice Boltzmann study of mass transfer for two-dimensional Bretherton/Taylor bubble train flow

A. Kuzmin^{*,a}, M. Januszewski^{b,d}, D. Eskin^c, F. Mostowfi^c, J.J. Derksen^a

^a*Chemical and Materials Engineering, University of Alberta
7th Floor, ECERF, 9107 116 St, Edmonton, Alberta, T6G 2V4 Canada*

^b*Institute of Physics, University of Silesia, 40-007 Katowice, Poland*

^c*Schlumberger DBR Technology Center
9450 17 Ave NW, Edmonton, Alberta, T6N 1M9 Canada*

^d*Google Switzerland GmbH, Brandschenkestrasse 110, 8002 Zurich, Switzerland*

Abstract

This work presents a procedure for the determination of the volumetric mass transfer coefficient in the context of lattice Boltzmann simulations for the Bretherton/Taylor bubble train flow for capillary numbers $0.1 < Ca < 1.0$. We address the case where the hydrodynamic pattern changes from having a vortex in a slug ($Ca < 0.7$) to not having it ($Ca > 0.7$) [1]. In the latter case the bubble shape is asymmetric and cannot be approximated through flat surfaces and circular circumferences as is often done in the literature [2, 3]. When the vortex is present in the slug, the scalar concentration is well mixed and it is common to use periodic boundary conditions and the inlet/outlet-averaged concentration as the characteristic concentration. The latter is not valid for flows where the tracer is not well mixed, i.e. $Ca > 0.7$. We therefore examine various boundary conditions (periodic, open, open with more than

*Corresponding author, Telephone: +1(438)824-3695

Email addresses: kuzmin@ualberta.ca (A. Kuzmin), michalj@gmail.com (M. Januszewski), deskin@slb.com (D. Eskin), fmostowfi@slb.com (F. Mostowfi), jos@ualberta.ca (J.J. Derksen)

1 unit cell) and definitions of the characteristic concentration to estimate mass transfer coefficients for the range of capillary numbers $0.1 < Ca < 1.0$. We show that the time-dependent volume averaged concentration taken as the characteristic concentration produces the most robust results and that all strategies presented in the literature are extreme limits of one unified equation. Finally, we show good agreement of simulation results for different Peclet numbers with analytical predictions of van Baten and Krishna [2].

Key words: Mass Transfer, Taylor/Bretherton bubble train flow, Multiphase flow, Lattice Boltzmann method, Binary liquid model, Flow in microchannels with parallel plates

1 1. Introduction

2 Monolith reactors have recently been getting more attention as a promis-
3 ing alternative to slurry reactors and trickle bed reactors [3, 4]. These re-
4 actors usually operate in the Bretherton-Taylor regime [5, 6] which is a flow
5 of equally sized, long air bubbles through a liquid medium, see Fig. 1. This
6 flow regime is characterized by the dominance of surface tension over inertia
7 and viscous effects, and by comparatively small gas flow velocities [7]. Due to
8 the dominance of surface tension, the flow exhibits advantageous properties
9 which cannot be achieved in its macroscopic counterparts: liquid thin films
10 [5] between bubbles and walls strongly enhance mass transfer from gas and
11 walls to liquid; the plug flow regime occurring in monolith reactors allows to
12 perform chemical reactions in slugs only [3]. Moreover, the low slip velocity
13 between gas and liquid is utilized in experiments to measure liquid velocity
14 [6]: bubbles travelling with approximately the same velocity as liquid can be

15 captured with a camera. These properties explain why nowadays one can find
 16 a large number of applications of the Bretherton-Taylor bubble train flow:
 17 continuous flow analyzers to measure liquid velocity, chemical reactors for
 18 hydrogenation of nitroaromatics, 2-ethyl-hexenal, Fischer-Tropsch synthesis,
 19 etc. The extensive reviews of Kreutzer et al. [3], Gupta et al. [8], Yue et al.
 20 [7] cover a significant number of applications.

This work is focused on gas to liquid mass transfer for the two-dimensional Bretherton/Taylor flow. A good understanding of mass transfer and how it depends on parameters such as the capillary number, the Reynolds number, and slug and bubble lengths allows to properly manufacture a microchannel with properties necessary to ensure that chemical reactions are performed in the best possible manner. The mass transfer coefficient is defined as the flux from the gas-liquid interface divided by the difference of the imposed concentration and the characteristic concentration in the domain. The concentration distribution in the domain is prescribed by underlying hydrodynamics fields. For example, experimental studies [7, 4] show a complex dependency of the mass transfer coefficient on flow parameters: bubble and slug lengths, and bubble velocity, which in turn relate to the capillary number Ca and the Reynolds number Re . Yue et al. [7] established an experimental correlation for the volumetric mass transfer coefficient for a bubble train as a function of the diffusion coefficient, slug and bubble lengths, and bubble velocity:

$$k_L a = \frac{2}{d_h} \left(\frac{DU_{\text{bubble}}}{L_{\text{bubble}} + L_{\text{slug}}} \right)^{0.5} \left(\frac{L_{\text{bubble}}}{L_{\text{bubble}} + L_{\text{slug}}} \right)^{0.3}, \quad (1)$$

21 where $k_L a$ is the volumetric mass transfer coefficient, d_h is the hydraulic
 22 diameter, L_{bubble} is the bubble length, L_{slug} is the slug distance (between
 23 bubbles), U_{bubble} is the bubble velocity, and D is the diffusion coefficient.

The understanding of mass transfer for the bubble train flow is not possible without knowledge of hydrodynamic patterns. There are several works studying the hydrodynamic properties of the bubble train flow, both experimental [9, 10, 11] and numerical [12, 13, 1, 14]. For the flow of long bubbles between parallel plates chosen here as the study case, it is indicated that there exists a vortex in the liquid slug for $Ca < 0.7$, and that the bubble shape is symmetric for low capillary numbers ($Ca < 0.1$ [11]) with the capillary number defined as:

$$Ca = \frac{\mu_{\text{liq}} U_{\text{bubble}}}{\gamma}, \quad (2)$$

where μ_{liq} is the liquid viscosity, U_{bubble} is the bubble velocity, and γ is the interfacial tension. The fact that the bubble shape for $Ca < 0.1$ can be represented as two hemicircles and two planar interfaces with the vortex existing in the liquid slug has been utilized for analytical estimations of mass transfer properties.

Since the mass transfer coefficient is defined in terms of a mass flux through a certain area, Eq. 5, analytical estimates [3, 15] are based on a decomposition of the bubble surface in parts. The mass transfer coefficient is calculated through two separate contributions from two planar films and two hemicircles. For both contributions the Higbie penetration theory [16] is utilized, which states that the mass transfer coefficient for a simple flow geometry depends on the average time a liquid packet interacts with a geometrical feature. It can be calculated as $\sqrt{\frac{\pi D}{t_{\text{char}}}}$, where t_{char} is the interaction time. As an example of the application of the Higbie penetration theory, the mass transfer coefficient for the flow of bubbles between parallel plates

is calculated as (similar to the work of van Baten and Krishna [2]):

$$k_L = 2\sqrt{\frac{\pi D}{t_{\text{film}}}} + 2\sqrt{\frac{\pi D}{t_{\text{circle}}}}, \quad (3)$$

where $t_{\text{film}} = \frac{L_{\text{film}}}{U_{\text{bubble}}}$ stands for the interaction time of liquid traveling next to the planar part of the bubble, and $t_{\text{circle}} = \frac{\pi R_{\text{circle}}}{U_{\text{bubble}}}$ is the time during which the liquid in the slug travels the distance of half the bubble cap circumference.

Despite their simplicity, such analytical expressions work well for flows with low capillary numbers $Ca < 0.1$ [4] where the bubble shape is symmetrical and can be approximated with good precision. Moreover, because of the hydrodynamic pattern in the slug (i.e. presence of a vortex in slug), one can estimate the time for a fluid batch to travel the whole circumference. However, with the increase of the capillary number the situation changes significantly – the symmetrical bubble shape is lost and the bubble resembles a bullet [17]. For flows with $Ca > 0.7$ there is also no vortex in the liquid slug. In this case the Higbie theory fails to estimate the contribution from bubble caps, which explains the need to turn to numerical simulations where all hydrodynamic fields as well as complex bubble shapes are taken into account.

Typical numerical studies of mass transfer [3, 2] do not consider the simulation of bubble shapes for $Ca > 0.1$. The usual simulation of mass transfer is performed as follows:

I The bubble shape is calculated either through analytical correlations [5] or experimental correlations [11] without directly resolving bubble shapes through multiphase simulations. The expressions for bubble shapes are available only for flows with capillary number $Ca < 0.1$.

51 **II** Hydrodynamic fields are then obtained by performing simulations of one-
52 component flow around the bubble by imposing the bubble velocity on
53 the channel walls. Thus, the simulations are performed in the reference
54 frame moving with the bubble. A stress-free condition is imposed at
55 the bubble surface.

III The mass transfer simulations are performed in the reference frame mov-
ing with the bubble. The saturation concentration is imposed at the
bubble surface. Only one unit cell containing a single bubble is used for
simulations. Periodic concentration boundary conditions are utilized to
determine the volumetric mass transfer coefficient, which is calculated
through the following equation [2]:

$$k_L a = \frac{\overline{\text{Flux}}}{C_{\text{bubble}} - \langle C_{\text{in/outlet}} \rangle} \frac{\text{bubble surface area}}{\text{unit cell volume}}, \quad (4)$$

56 where $\langle C_{\text{in/outlet}}(t) \rangle = \int C U_{\text{in/outlet}} dA / \int U_{\text{in/outlet}} dA$ is the space-averaged
57 inlet/outlet (periodic boundary conditions) concentration as a function
58 of time. Therefore, in terms of the mass transfer definition, $\langle C_{\text{in/outlet}}(t) \rangle$
59 plays the role of the characteristic concentration. The time-averaged
60 concentration flux ($\overline{\text{Flux}}$) is calculated as the difference between the
61 overall average concentration in the whole domain ($\langle C_{\text{overall}} \rangle = \int_V C dV / V$)
62 at time t_1 and at time t_2 divided by the time difference $t_2 - t_1$. The
63 agreement between numerical simulations [2] and experimental corre-
64 lations of Bercic and Pintar [4] was good.

65 The presented numerical approaches [2, 3] can be criticized on a number of
66 points. They mainly relate to the bubble shape approximation, which is taken
67 to be symmetrical, i.e. consisting of two hemispheres and film for the case

68 of flow in circular capillaries. This is valid for small capillary numbers only
 69 ($Ca < 0.1$). As previously discussed, for such capillary numbers the tracer
 70 is well mixed in the slug and the choice of the characteristic concentration
 71 needed for the mass transfer coefficient, Eq. 5, is obvious. With minimal
 72 differences in the results, it can either be the averaged concentration in the
 73 liquid slug or the inlet/outlet space-averaged concentration. The latter is
 74 used in the formulation of van Baten and Krishna [2] presented above.

75 While it is clear that periodic boundary conditions can be employed for
 76 the calculation of hydrodynamic fields, the same does not apply to the mass
 77 transfer coefficient simulations. Experimental correlations [4] show that the
 78 concentration in a bubble train along the streamwise direction changes ex-
 79 ponentially with distance. Mass transfer simulations however, are made only
 80 for one unit cell using periodic boundary conditions with the same concen-
 81 tration at the inlet and at the outlet. The question is how single unit cell
 82 simulation corresponds to experimental measurements arises where concen-
 83 tration difference is measured at the distances of at least a few unit cells [4].
 84 In other words, one needs to understand how the discrete one unit cell simu-
 85 lation corresponds to the continuous picture in experiments where one does
 86 not distinguish discrete bubbles but takes measurements of concentration at
 87 different locations.

88 Addressing situations for a rich number of hydrodynamic patterns, shapes,
 89 and effects of bubble lengths, etc for bubble train flows, we feel that there is
 90 a need to examine carefully the strategies and assumptions behind the nu-
 91 merical calculations of the mass transfer coefficient. We aim at establishing
 92 clear procedures as to how properly obtain the mass transfer coefficient via a

93 study of different boundary conditions and different definitions of the char-
 94 acteristic concentration. The case we want to examine is a two-dimensional
 95 bubble train flow between parallel plates. We address the following issues:

96 **I** Applicability of periodic boundary conditions to determine the mass trans-
 97 fer coefficient when the vortex in the slug disappears, i.e. when $Ca >$
 98 0.7 .

99 **II** Validity of the inlet/outlet-averaged or domain-averaged concentrations
 100 as characteristic concentrations in the definition of the mass transfer
 101 coefficient.

102 **III** Translation of the continuous experimental picture to numerical simu-
 103 lations of a few unit cells, the issue of correspondence between space
 104 averages (simulations [2]) and time averages (experiment).

105 In addition, at the end of the manuscript we present results of the depen-
 106 dence of the volumetric mass transfer coefficient on the Peclet number that we
 107 compare with analytical [15] and experimental correlations [7]. The thorough
 108 determination of the mass transfer coefficient and associated Sherwood num-
 109 ber as a function of other non-dimensional parameters such as gas holdup,
 bubble/slug lengths, and the capillary number is left for future studies.

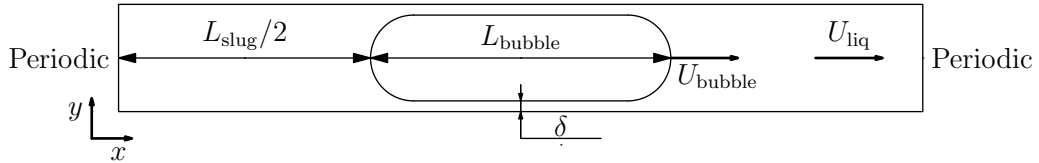


Figure 1: Simplified sketch of the bubble motion. Using periodic conditions for the velocity field is natural, but needs evaluation for mass transfer.

110

111 To establish numerical procedures we performed multiphase simulations
112 to extract bubble shapes [17, 13] for the range of capillary numbers $Ca =$
113 $0.1 \div 1.0$. For this range of capillary numbers we were able to capture the
114 bubble shape change and the change of hydrodynamic patterns. The mass
115 transfer simulations presented here were performed with various boundary
116 conditions (open, periodic) and with a few unit cells (1 to 10 unit cells). As
117 our numerical approach we take the lattice Boltzmann method, a relatively
118 new CFD competitor developed during last 20 years [18, 19, 20, 21]. This
119 method was successfully applied to simulate not only single phase hydro-
120 dynamic problems [22], but also multiphase flows [23, 24, 25], heat transfer
121 [26, 27], and ferrofluids [28, 29].

122 Mass transfer problems in the lattice Boltzmann framework were mainly
123 addressed in a series of works of Ginzburg and co-authors [30, 31, 32]. In con-
124 trast to these works whose focus was on simulating the advection-diffusion
125 equation via the lattice Boltzmann framework, we concentrate on the ap-
126 plication side. One should also mention the work of Yoshino and Inamuro
127 [33] about heat and mass transfers in porous media and the work of Derksen
128 [34] simulating lateral mixing in cross-channel flow. The last two works are
129 focused on problems of homogeneous nature and do not provide guidance as
130 to how to obtain the mass transfer coefficient for heterogeneous cases.

131 The paper is organized as follows. We start with definitions of the volu-
132 metric mass transfer coefficient and apply them to the bubble train flow to
133 derive expressions to connect the space- and time-averages. Then, the lattice
134 Boltzmann model used to simulate mass transfer is presented, followed by

135 benchmarks. Finally, numerical simulations of various boundary conditions
 136 and simulations spanning a few unit cells for different hydrodynamic pat-
 137 terns are presented to establish the procedure to determine the volumetric
 138 mass transfer coefficient. The comparison with analytical correlations is also
 139 presented.

140 2. Mass transfer definitions

By definition, the mass transfer coefficient from a surface with an imposed constant concentration C_{bubble} is:

$$k_L = \frac{\dot{m}}{P\Delta C}, \quad \Delta C = C_{\text{bubble}} - C_{\text{medium}}, \quad (5)$$

141 where \dot{m} is the mass flux $\left[\frac{kg}{s}\right]$, P is the area of the surface $\left[m^2\right]$, and ΔC is
 142 the concentration difference between the surface and the surrounding medium
 143 $\left[\frac{kg}{m^3}\right]$. Therefore, k_L has a dimension of $\left[\frac{m}{s}\right]$. Usually, the surrounding
 144 medium concentration is taken at an infinite distance from the bubble. How-
 145 ever, in the case of complicated geometries and non-homogeneous concen-
 146 trations, the medium concentration can be the average concentration in the
 147 domain or the flux-averaged concentration at the inlet or outlet, etc. Thus,
 148 one needs to establish a clear definition of ΔC to determine the volumetric
 149 mass transfer coefficient in the case of complex geometries and non-trivial
 150 hydrodynamic velocity patterns.

151 We first examine the definitions of mass transfer in the case of point
 152 sources.

153 *2.1. Point mass sources*

154 In what follows we will present three approaches to calculate point mass
 155 transfer coefficients (by point source we assume the source to have an in-
 156 finitesimally small surface area P):

1. Let us look at the infinitesimally small domain of volume $A\Delta x$, not moving and containing a point source. The concentration difference is $\Delta C = C^* - C(t)$, where C^* is the imposed point source concentration, and $C(t)$ is the time-dependent concentration, which does not depend on the location due to the assumption of homogeneity. One can therefore write a time-dependent ordinary differential equation for the concentration in the domain:

$$\dot{m} = A\Delta x \frac{dC}{dt} = k_L P (C^* - C(t)), \quad (6)$$

with the initial condition $C(0) = 0$. The solution can be found as:

$$C(t) = C^* (1 - \exp(-k_L a t)), \quad (7)$$

where $k_L a$ is the volumetric mass transfer coefficient defined as:

$$k_L a = k_L \frac{P}{A\Delta x} = k_L \frac{P}{V}, \quad (8)$$

157 where P is the source surface, V is the unit cell volume.

- 158 2. Let us predict mass transfer in a liquid moving with the velocity U , see
 159 Fig. 2.

If one can assume that the point mass sources are distributed in the whole medium, the mass accumulated in the volume $V = A\Delta x$ can be calculated as the difference of mass fluxes entering and leaving the

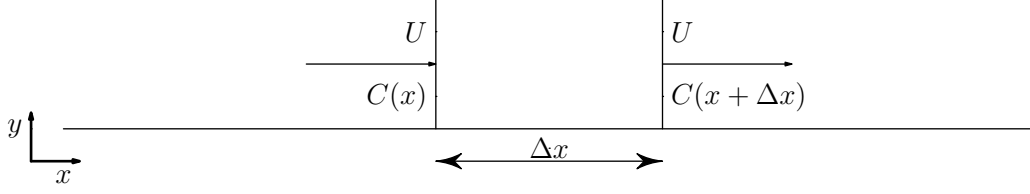


Figure 2: The mass transfer in a moving liquid.

domain $U(C(x + \Delta x) - C(x))$. The accumulated mass should be proportional to the mass transfer coefficient:

$$U(C(x + \Delta x) - C(x)) = k_L P(C^* - C(x)), \quad (9)$$

giving the same solution but only in the spatial domain:

$$C(x) = C^* \left(1 - \exp\left(-k_L a \frac{x}{U}\right) \right). \quad (10)$$

160 Note that the concentration $C(x)$ does not depend on time.

161 3. If one transfers to the frame moving with the liquid velocity U , the
 162 situation will be the same as in the first case. One can connect time
 163 and space with the velocity U ($t = \frac{x}{U}$) to obtain the same equation as
 164 in the case 2.

165 2.2. Bubble train

166 In the application to the bubble train flow it is useful to think of one
 167 bubble as a point source to be able to use the calculations presented above.
 168 For example, the expression (10) was used in experiments by Bercic and
 169 Pintar [4]. However, one should be accurate with the definition of velocities
 170 because two different phases co-exist in the bubble train flow. Usually, one
 171 can take the velocity U to be a bulk velocity or $U = U_{\text{gas}} + U_{\text{liq}}$, where U_{gas}
 172 and U_{liq} are liquid and gas superficial velocities, respectively.

173 With experimental measurements of concentration at different locations,
 174 the calculation of the mass transfer coefficient using the logarithmic func-
 175 tion is straightforward. However, if one wants to analytically or numerically
 176 calculate the mass transfer coefficients, the situation is much more compli-
 177 cated because of the presence of two phases and complex bubble geometry.
 178 As was mentioned before, depending on the capillary number the velocity
 179 pattern and thus scalar mixing is different. Analytical approaches [15, 2]
 180 assume that the contributions from film and bubble caps can be calculated
 181 separately. Therefore no tracer from the film influences bubble caps diffu-
 182 sion. However, this assumption overpredicts mass transfer for a number of
 183 experiments [15]. This happens since some tracer concentration from the
 184 film is mixed with the slug and increases the overall concentration in the
 185 slug, thereby decreasing the mass transfer from the bubble caps. Therefore,
 186 the analytical estimates for the mass transfer coefficient calculation do not
 187 account for mutual mass transfer from neighbouring bubbles.

188 Overall, mixing patterns of the film and liquid slugs are of great im-
 189 portance for the estimation of mass transfer [7]. However, the assumptions
 190 usually taken for mass transfer calculations are small capillary numbers and
 191 certain mixing patterns such as to help to estimate the mass transfer using
 192 the penetration theory of Higbie [16].

193 In comparison with analytical calculations and simplifications, the nu-
 194 merical approach can take into account the complex mixing patterns and
 195 geometries. However, there are challenges as how to mimic the continuous
 196 picture where the medium is moving with bulk velocity $U = U_{\text{gas}} + U_{\text{liq}}$ as
 197 it is done in experiments. Thus, the questions indicated in Section 1 arise.

198 The next section gives more details about numerical simulations.

199 *2.3. Numerical simulations*

200 Ideally one wants to mimic the continuous picture as it is seen in ex-
 201 periments. Thus, mass transfer simulations for a number of unit cells each
 202 containing a bubble are needed. As was indicated above, there are two ap-
 203 proaches towards it – either to simulate the bubble train and then to measure
 204 concentration along the pipe, Eq. 10, or to transfer to the reference frame
 205 moving with the bulk velocity U and conduct the same measurements. How-
 206 ever, both methods require tracking of moving bubbles which is complicated
 207 from the numerical point of view. Therefore, one needs to come up with a
 208 simple and smaller domain for calculations of the mass transfer coefficient,
 209 which closely mimics the continuous picture of a large number of separated
 210 bubbles.

211 To avoid complications with moving grids, our approach is to simulate
 212 mass transfer in a reference frame moving with the bubble. Therefore, one
 213 needs to examine Eq. 10 more closely.

We perform simulations in the frame co-moving with the bubble in which
 the bubble position stays constant. The bubble velocity U_{bubble} is different
 from the bulk velocity $U = U_{\text{gas}} + U_{\text{liq}}$, and one thus needs to perform a x
 coordinate variable change:

$$\begin{aligned}
 x(t) &= U_{\text{bubble}} t \\
 \overline{C(x)} &= C^* \left(1 - \exp \left(-k_L a \frac{x}{U_{\text{gas}} + U_{\text{liq}}} \right) \right) \\
 \langle C(t) \rangle &= C^* \left(1 - \exp \left(-k_L a t \frac{U_{\text{bubble}}}{U_{\text{gas}} + U_{\text{liq}}} \right) \right),
 \end{aligned} \tag{11}$$

where $\langle C(t) \rangle$ is the space-averaged characteristic concentration, and $\overline{C(x)}$ is the time-averaged concentration at location x . One can make different choices for $\langle C(t) \rangle$ such as the concentration averaged over the whole domain or inlet/outlet space-averaged concentrations used in works [2, 3]. The volumetric mass transfer coefficient can be obtained through the space-averaged concentration:

$$\begin{aligned} k_L a t \frac{U_{\text{bubble}}}{U_{\text{gas}} + U_{\text{liq}}} &= \ln \frac{C^*}{C^* - \langle C(t) \rangle} \\ k_L a \frac{L_{\text{unit}}}{U_{\text{bubble}} + U_{\text{gas}}} &= \frac{L_{\text{unit}}}{U_{\text{bubble}} t} \ln \frac{C^*}{C^* - \langle C(t) \rangle}, \end{aligned} \quad (12)$$

where the parameter $k_L a \frac{L_{\text{unit}}}{U_{\text{gas}} + U_{\text{liq}}}$ is non-dimensional. One can also measure the volumetric mass transfer coefficient from concentrations given at times t_1 and t_2 :

$$k_L a \frac{L_{\text{unit}}}{U_{\text{bubble}} + U_{\text{gas}}} = \frac{L_{\text{unit}}}{U_{\text{bubble}}(t_2 - t_1)} \ln \frac{C^* - \langle C(t_1) \rangle}{C^* - \langle C(t_2) \rangle}. \quad (13)$$

214 Expressions (11 - 13) are the cornerstones of the present work . Four possible
215 scenarios of numerical simulations have been examined:

- 216 1. One unit cell is simulated with periodic boundary conditions, see Fig.
217 3. In this case no tracer leaves the domain similarly to the plug flow.
218 Though easier to implement, it gives rise to the criticism that the inlet
219 concentration is equal to the outlet one. As was discussed, in exper-
220 iments there is a concentration difference between the inlet and the
221 outlet, even for one unit cell.

In this case, the volumetric mass transfer coefficient is calculated by Eq. 12. The characteristic concentration $\langle C(t) \rangle$ required for the volumetric mass transfer coefficient is taken as the average concentration in the

domain:

$$C(t) = \frac{\int_{liquid} C dV}{\int dV}. \quad (14)$$

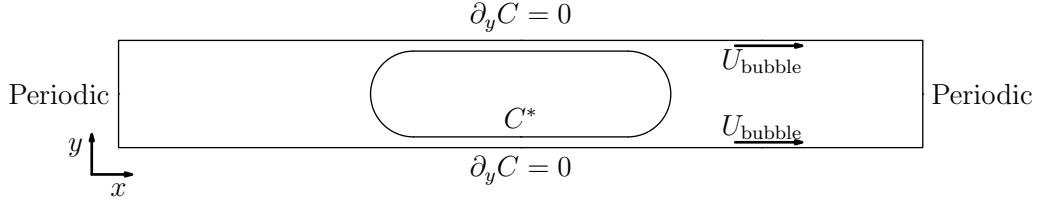


Figure 3: The two-dimensional benchmarks for the mass transfer coefficient (bottom) for the bubble located near the entrance (top) and at the middle of the domain (bottom).

222

2. Periodic boundary conditions are applied as in the first case but the characteristic concentration is taken as the inlet/outlet flux-averaged concentration [2]:

$$\begin{aligned} \langle C_{\text{inlet}}(t) \rangle &= \frac{\int U(y)C(0, y, t)dy}{\int U(0, y)dy} \\ \langle C_{\text{outlet}}(t) \rangle &= \frac{\int U(y)C(L_{\text{unit}}, y, t)dy}{\int U(L_{\text{unit}}, y)dy} \end{aligned} \quad (15)$$

$$C_{\text{inlet}}(\mathbf{x}, t) = C_{\text{outlet}}(\mathbf{x}, t), \text{ due to periodicity.}$$

223

224

225

226

The assumptions of this approach are that the concentration difference between the inlet/outlet- and the space-averaged over the whole unit cell is not significant. Thus, the tracer is assumed to be well mixed in the slug.

3. The approach of van Baten and Krishna [2], where periodic boundary conditions are used and the mass transfer coefficient is calculated as the

gain of the mass in the system divided by the concentration difference multiplied by the surface area:

$$k_L a = \frac{\dot{m}}{P \Delta C} \frac{P}{V} = \frac{\dot{m}}{V(C^* - \langle C(t) \rangle)}, \quad (16)$$

where the mass flux in the domain can be calculated as:

$$\dot{m} = \frac{m_2 - m_1}{t_2 - t_1} = \frac{\int_{liq} C(\mathbf{x}, t_2) d\mathbf{x} - \int_{liq} C(\mathbf{x}, t_1) d\mathbf{x}}{t_2 - t_1}. \quad (17)$$

In the approach of van Baten and Krishna the inlet/outlet flux-averaged concentrations were taken as the characteristic concentration $\langle C(t) \rangle$.

4. Simulation of several unit cells, see Fig. 4. This situation corresponds to the head of the bubble train, after injection in the pipe and traveling along the channel. One can see that this situation best resembles the experimental picture, but also requires larger computational resources. By simulating a certain number of bubbles in the train head, the influence of the boundaries can be reduced. For example, left and right boundary conditions in this case are taken as open boundaries, i.e. $\partial C / \partial x = 0$. There is no ambiguity in the choice of the characteristic concentration. The average concentration of any unit cell far away from boundaries will be governed by Eq. 13.

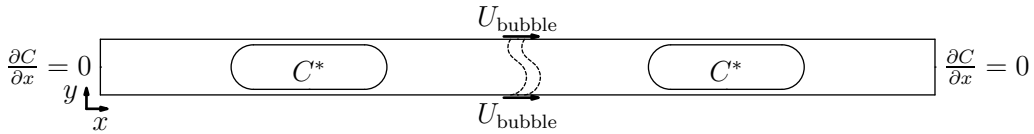


Figure 4: Benchmark for multiple unit cells.

One can notice that all examined cases are the extreme limits of one equation:

$$k_L a = \frac{\dot{m} - \int C_{\text{outlet}}(t)u(L_{\text{unit}}, y)dy + \int C_{\text{inlet}}(t)u(0, y)dy}{V\Delta C}, \quad (18)$$

where $\Delta C = C^* - \langle C(t) \rangle$ with $\langle C(t) \rangle$ taken to be the average concentration in the whole liquid domain, \dot{m} is the mass gain in the domain, $\int C_{\text{inlet}}u(0, y)dy$ and $\int C_{\text{outlet}}u(L_{\text{unit}}, y)dy$ are inlet/outlet mass fluxes. Eq. 18 describes the mass balance: whatever was generated by the bubble surface equals the domain mass change minus whatever left the domain plus whatever entered it.

Periodic boundary conditions are the extreme limiting case of Eq. 18:

$$\int C_{\text{outlet}}(t)u(L_{\text{unit}}, y)dy = \int C_{\text{inlet}}(t)u(0, y)dy.$$

Another limiting case (will be shown later) is when the mass accumulation rate equals zero, i.e. $\dot{m} = 0$. This situation corresponds to a simulation of a few unit cells with open boundary for flows with $Ca > 0.7$.

Before we examine all the test cases above, some lattice Boltzmann mass transfer benchmarks will be presented.

3. Validation

As was discussed earlier, analytical correlations for the mass transfer coefficient have been derived for a Taylor bubble train flow as two separate contributions: the mass transfer from two half circles and the mass transfer from the film. We will examine these mass transfer cases closely with the

255 help of the lattice Boltzmann method and compare them against analyti-
 256 cal solutions. The next sections will give a short introduction to the lattice
 257 Boltzmann method and present benchmark results.

258 3.1. TRT D2Q9 model

The lattice Boltzmann equation (LBE) operates on a square/cubic grid representing the physical domain. It utilizes probability distribution functions (also known as particle populations) containing information about macroscopic variables, such as fluid density and momentum. LBE consists of two parts: a local collision step, and a propagation step which transports information from one node to another along directions specified by a discrete velocity set. The LBE is typically implemented as follows:

$$\begin{aligned} f_i^*(\mathbf{x}, t) &= f_i(\mathbf{x}, t) - \omega(f_i(\mathbf{x}, t) - eq_i(\mathbf{x}, t)), & \text{collision step} \\ f_i(\mathbf{x} + \mathbf{c}_i, t + 1) &= f_i^*(\mathbf{x}, t), & \text{propagation step,} \end{aligned} \quad (19)$$

259 where f_i is the probability distribution function in the direction \mathbf{c}_i , eq_i is
 260 the equilibrium probability distribution function, and ω is the relaxation
 261 parameter. The term $-\omega(f_i - eq_i)$ is the so-called BGK collision operator
 262 [35]. However, the approach used here is the TRT (two-relaxation-times)
 263 collision operator [30, 32]. In comparison with the widely used BGK collision
 264 operator, the TRT collision operator has better accuracy for diffusion and
 265 convection fluxes, as well as a larger range of parameters where the scheme
 266 is stable.

The TRT collision operator [36] decomposes the populations and the equilibrium distribution into a symmetric and an antisymmetric part:

$$f_i^\pm = \frac{f_i \pm f_{\bar{i}}}{2}, \quad eq_i^\pm = \frac{eq_i \pm eq_{\bar{i}}}{2}, \quad (20)$$

where \bar{i} is the opposite direction to the i -th direction. The collision is performed with two independent relaxation rates for symmetric and antisymmetric modes:

$$\begin{aligned} f_i^*(\mathbf{x}, t) &= f_i(\mathbf{x}, t) - \omega_+(f_i^+ - eq_i^+) - \omega_-(f_i^- - eq_i^-) \\ f_i(\mathbf{x} + \mathbf{c}_i, t + 1) &= f_i^*(\mathbf{x}, t). \end{aligned} \quad (21)$$

267 Note that the TRT collision operator reduces to the BGK operator if $\omega_+ =$
 268 ω_- . In comparison with the BGK collision operator, the TRT collision oper-
 269 ator has one additional degree of freedom. The TRT operator introduces the
 270 following free parameter $\Lambda = \left(\frac{1}{\omega_+} - \frac{1}{2}\right)\left(\frac{1}{\omega_-} - \frac{1}{2}\right)$. This free parameter con-
 271 trols the effective location of bounce-back walls [37], second-order accuracy
 272 of boundary [36] and interface schemes [38], spatial accuracy [39, 40], con-
 273 sistency [41] and, to some extent, stability [42, 43, 40]. In particular, $\Lambda = \frac{1}{4}$
 274 achieves the optimal stability for the isotropic advection-diffusion equation
 275 [42].

The parameters ω_+ , ω_- and eq_i fully define the lattice Boltzmann procedure. The two-dimensional, nine-velocity LBM $D2Q9$ we used in this work is defined on the set of lattice velocities with components:

$$\begin{aligned} c_{ix} &= \{0, 1, 0, -1, 0, 1, -1, -1, 1\}, \text{ for } i = 0 \dots 8 \\ c_{iy} &= \{0, 0, 1, 0, -1, 1, 1, -1, -1\}, \text{ for } i = 0 \dots 8. \end{aligned} \quad (22)$$

The equilibrium functions for the $D2Q9$ TRT model are represented as

[42]:

$$\begin{aligned}
eq_i^+ &= eq_i^{(m)} + g^{(u)} eq_i^{(u)} \\
eq_i^{(m)} &= t_i^{(m)} c_e + eq_i^{(a)} \\
eq_i^{(u)} &= t_i^{(u)} \frac{u_x^2 + u_y^2}{2} + \frac{u_x^2 - u_y^2}{4} p_i^{(xx)} + g_{xy}^{(u)} \frac{u_x u_y}{4} p_i^{xy} \\
eq_i^{(a)} &= \frac{K_{xx} - K_{yy}}{4} p_i^{xx} + \frac{K_{xy}}{4} p_i^{(xy)} \\
eq_i^- &= t_i^{(a)} u_\alpha c_{i\alpha},
\end{aligned} \tag{23}$$

where $K_{xx,yy,xy}$ are proportional to components of the diffusion tensor, $c_e = \frac{K_{xx} + K_{yy}}{2}$, parameters $g^{(u)}$ and g_{xy}^u are either zero or one (see below), the tensor $p_i^{(xx)} = c_{ix}^2 - c_{iy}^2$, the tensor $p_i^{(xy)} = c_{ix} c_{iy}$, the weights $t_i^{(u,m,a)}$ can be chosen based on stability criteria. The most commonly used set of weights, the so-called “hydrodynamic” weights, were chosen:

$$t_i^{(u)} = t_i^{(m)} = t_i^{(a)} = \left\{ 0, \frac{1}{3}, \frac{1}{3}, \frac{1}{3}, \frac{1}{3}, \frac{1}{12}, \frac{1}{12}, \frac{1}{12}, \frac{1}{12} \right\} \tag{24}$$

It can be shown through the Chapman-Enskog procedure [44], that the simple update rule with the equilibrium function presented above restores the anisotropic advection-diffusion equation:

$$\partial_t C + \partial_\alpha C u_\alpha = \partial_{\alpha\beta} D_{\alpha\beta} C, \tag{25}$$

where the concentration $C = \sum_i f_i$, and $D_{\alpha\beta} = \left(\frac{1}{\omega_-} - \frac{1}{2} \right) K_{\alpha\beta}$ is the following diffusion tensor:

$$D_{\alpha\beta} = \begin{pmatrix} D_{xx} + \left(\frac{1}{\omega_-} - \frac{1}{2} \right) (g^{(u)} - 1) u_x^2 & D_{xy} + \left(\frac{1}{\omega_-} - \frac{1}{2} \right) (g_{xy}^{(u)} - 1) u_x u_y \\ D_{xy} + \left(\frac{1}{\omega_-} - \frac{1}{2} \right) (g_{xy}^{(u)} - 1) u_x u_y & D_{yy} + \left(\frac{1}{\omega_-} - \frac{1}{2} \right) (g^{(u)} - 1) u_y^2 \end{pmatrix} \tag{26}$$

276 We want to resolve the isotropic advection-diffusion equation, $D = D_{xx} =$
277 D_{yy} or $K = K_{xx} = K_{yy}$, with the non-diagonal diffusion tensor components

278 set to zero ($D_{xy} = 0$). In contrast to the $D2Q5$ model, with $D2Q9$ it is possi-
 279 ble to cancel the numerical diffusion by the proper choice of the equilibrium
 280 functions, i.e. $g_{xy}^{(u)} = g^{(u)} = 1$. The particular choice of parameters used in
 281 simulations is $c_e = \frac{1}{3}$, $\Lambda = \frac{1}{4}$. Thus, the diffusion coefficient D is matched
 282 through ω_- , i.e. $D = c_e \left(\frac{1}{\omega_-} - \frac{1}{2} \right) = \frac{1}{3} \left(\frac{1}{\omega_-} - \frac{1}{2} \right)$. For the particular choice
 283 $\Lambda = \frac{1}{4}$, ω_+ can be found easily as $\omega_+ = 2 - \omega_-$.

We validated two types of boundary conditions: Inamuro boundary condi-
 tions [33] and pressure anti bounce-back boundary conditions [37]. However,
 the simulation results are presented only for pressure anti bounce-back due
 to their ability to handle complex boundaries in a simple way:

$$f_{B,i}^* = -f_{F,\bar{i}}^* + 2eq^+(C^*, \mathbf{u}), \quad (27)$$

284 where C^* is the concentration to be imposed at the surface, \mathbf{u} is the surface
 285 velocity, i is the direction number pointing to the domain located at the
 286 boundary surface B , \bar{i} is the direction number opposite to i and is located at
 287 the fluid node F specifically so that node B is located at the location $F + \mathbf{c}_i$.

288 Note that the parameters of the lattice Boltzmann scheme are connected
 289 with physical parameters only through non-dimensional numbers governing
 290 the physics of the problem. In our case, this number is the Peclet number,
 291 $Pe = \frac{U_{\text{bubble}} L}{D}$. Therefore, one can choose any quantity, for example U_{bubble}
 292 in the lattice Boltzmann units as long as the Peclet number is matched in
 293 physical space and numerical simulations. The fact that U_{bubble} can be varied
 294 in certain ranges is extremely useful in the context of numerical simulations.
 295 This allows to increase the time step and decrease the computational demand
 296 (by an order of magnitude). This point will be used in simulations and
 297 covered later.

298 The next section will cover LBM benchmarks that resemble the mass
 299 transfer from a bubble (mass transfer to the liquid with the parabolic velocity
 300 profile and mass transfer from a cylinder).

301 3.2. The radial case

The case to be examined is the mass transfer from a circle with radius a , with the circle approximated as a stair-case. It can be described by the following system of equations:

$$\begin{aligned}\partial_t C(r, t) &= \frac{1}{r} \partial_r r \partial_r C(r, t) \\ C(a, t) &= C_0, \quad C(r, 0) = C_{init}\end{aligned}\tag{28}$$

The analytical solution is [45]:

$$\frac{C(r, t) - C_0}{C_{init} - C_0} = \sum_{n=1}^{\infty} \frac{2}{\mu_n J_1(\mu_n)} \exp\left(-\mu_n^2 \frac{Dt}{a^2}\right) J_0\left(\mu_n \frac{r}{a}\right),\tag{29}$$

where μ_n is the n -th zero root of the 0th order Bessel polynomial $J_0(\mu_n) = 0$. Some of the corresponding roots are as follows: $\mu_1 = 2.4048$, $\mu_2 = 5.5201$, $\mu_3 = 8.6537$, $\mu_4 = 11.7915$, $\mu_5 = 14.9309$. By taking the initial concentration as 0, one obtains:

$$C(r, t) = C_0 \left(1 - \sum_{n=1}^{\infty} \frac{2}{\mu_n J_1(\mu_n)} \exp\left(-\mu_n^2 \frac{Dt}{a^2}\right) J_0\left(\mu_n \frac{r}{a}\right) \right).\tag{30}$$

302 The solution depends only on the non-dimensional time: $\tau = \frac{Dt}{a^2}$. The
 303 domain size was 129×129 with the circle radius $a = 40$ lattice units. Some re-
 304 sults for different diffusion coefficients are presented in Fig.5. The numerical
 305 simulations with the bounce-back boundary conditions are able to accurately
 306 reproduce the analytical results.

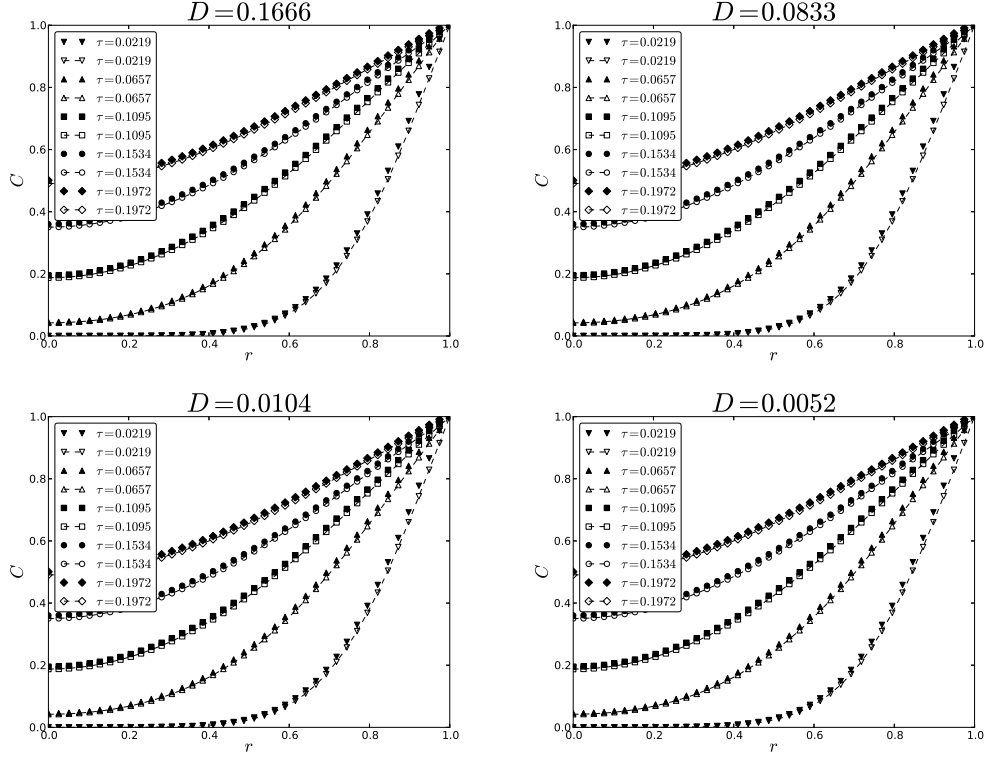


Figure 5: Profiles for different diffusion parameters varied with ω_- (lines: Eq. 30, symbols: LB results). One can see that the diffusion from curved boundaries is captured accurately . r is the distance from the center.

3.3. Poiseuille velocity profile

The problem we want to address can be formulated through the following PDE:

$$\begin{aligned}
 \frac{\partial C}{\partial x} U(y) &= D \frac{\partial^2 C}{\partial y^2} \\
 C(0, y) &= 0, \quad C(x, \pm\delta) = C^*, \quad \frac{\partial C}{\partial y}(x, 0) = 0 \\
 U(y) &= U_0 \left(1 - \left(\frac{y}{\delta} \right)^2 \right)
 \end{aligned} \tag{31}$$

The procedure to solve this problem is presented in Appendix A which yields the final solution as:

$$C = C^* - C^* \sum_{m=0} C_m e^{-m^4 \frac{x}{\delta} \frac{1}{Pe}} e^{-m^2 y^2 / (2\delta^2)} {}_1F_1\left(-\frac{m^2}{4} + \frac{1}{4}, \frac{1}{2}, m^2 \frac{y^2}{\delta^2}\right), \quad (32)$$

where coefficients C_m are taken from Eq. 48. The comparison between contours of analytical and simulation results is presented in Fig. 6. Parameters were taken as: $D = 0.0185$, the grid dimension is 80×1600 . The centerline velocity is $U_0 = 0.05$ which yields the Peclet number $Pe = U_0 \delta / D = 108.108$. The results are in good agreement. The simulations capture accurately the singular derivative for $x = 0$.

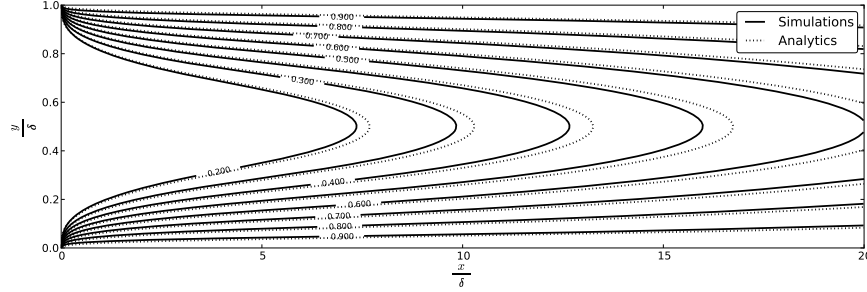


Figure 6: Comparison between the analytical concentration contours and simulations with pressure anti bounce-back conditions, Eq. 27. The simulation was done for $D = 0.0185$ with a 80×1600 grid. The centerline velocity is $U_0 = 0.05$, and the Peclet number is 108.108.

313

314 Now the LBM is validated against the benchmarks relevant for the flow
315 around bubbles, one can examine the cases mentioned in Section 2.3 to cal-
316 culate the volumetric mass transfer coefficient for Taylor bubble train flow.

317 4. Numerical approach

318 A multiphase code was utilized to obtain the flow patterns and bubble
 319 shapes for different capillary numbers [17]. Five particular cases were cho-
 sen to be examined, their results are summarized in Table 1. Note that

Ca	Re	U_{bubble}	δ	ε_{gas}	U_{liq}	U_{gas}	L_{bubble}	L_{slug}
0.097	1.656	0.0055	0.092	0.30	0.0046	0.0016	5.79	9.21
0.254	4.318	0.0143	0.132	0.28	0.0108	0.0041	6.12	8.88
0.526	8.938	0.0297	0.157	0.27	0.0209	0.0080	6.19	8.81
0.750	12.744	0.0424	0.167	0.25	0.0293	0.0107	5.96	9.04
1.040	17.665	0.0588	0.177	0.22	0.0397	0.0135	5.59	9.41

Table 1: Sample results with the binary liquid lattice Boltzmann model [17]. The following notations are used: the capillary number $Ca = \frac{U_{\text{bubble}}L}{\rho\nu_{\text{liq}}}$, U_{liq} is the superficial liquid velocity, U_{gas} is the superficial gas velocity. δ is the non-dimensional film thickness, L_{bubble} and L_{slug} are the non-dimensional bubble and slug lengths (defined in channel heights). The simulation sketch is presented in Fig. 1.

320

321 the velocities (LB system) in Table 1 are small. This means that to match
 322 large Peclet numbers, $Pe = \frac{U_{\text{bubble}}L}{D}$, usually used in experiments, one needs
 323 to decrease the diffusion coefficient $D = \frac{1}{3}\left(\frac{1}{\omega_-} - \frac{1}{2}\right)$. Thus, the parame-
 324 ter $\omega_- \approx 0.5$. However, for such values of ω_- the stability of the lattice
 325 Boltzmann method drastically decreases [43]. On the other hand, one iter-
 326 ation in the lattice Boltzmann system corresponds to a physical time step
 327 $\Delta t = U_{\text{bubble, LB}} \frac{\Delta x}{U_{\text{bubble, phys}}}$. The iteration time is proportional to the velocity
 328 U_{LB} and the typical number of simulation steps to obtain the steady-state
 329 mass transfer coefficient for $Ca < 0.2$ is of the order of a few million. There-
 330 fore, it is desirable to increase U_{LB} while maintaining the Peclet number. If

one increases the velocity, then ω_- increases as well, which impacts positively on the stability of the LBM.

Given all the considerations above, mass transfer simulations are performed as follows:

Flow field Given a capillary number Ca , one needs to obtain hydrodynamic fields around the bubble using the multiphase binary liquid lattice Boltzmann model according to our previous work [17]. Periodic boundary conditions were used in that work. The grid used was 202×3000 which corresponds to the fluid domain of size 200×3000 . That grid resolution was taken to ensure grid independency of the results [17]. Note that we do not approximate bubble shapes by correlations, but we directly resolve them by using the multiphase solver.

Bubble reference frame Once the hydrodynamics is solved, the mass transfer simulations are conducted in the reference frame moving with the bubble, where the bubble stands still and the liquid flows around the bubble. We impose a uniform and steady concentration on the surface of the bubble with the anti bounce-back condition, Eq. 27.

Velocity improvement One can scale the velocity to perform faster simulations. However, before doing it one needs to improve the velocity field. This issue arises because of the multiphase model used in the flow simulations. The binary liquid lattice Boltzmann model is a diffuse interface model where no clear boundary between gas and liquid exists. We obtain the bubble shape by imposing a condition on the order parameter field ϕ with $\phi \leq 0$ in the bubble [17]. The velocity of

the bubble is defined as the bubble tip velocity. Because of the square grid, the shape of the bubble is determined within an accuracy of one grid spacing. Thus, there is an error in the determination of the bubble velocity. Though these errors are small, there is still a small non-zero velocity component pointing into the bubble in some places, see Fig. 8 in [17] where some streamlines are penetrating the bubble surface. This small velocity is amplified upon the velocity scaling and is inconsistent with the advection-diffusion equation leading to instability after many iterations.

Thus, before performing the mass transfer simulations an additional single phase hydrodynamic simulation is performed. A free-surface solver was developed in order to obtain a velocity field consistent with the advection-diffusion equation. We take results from the multiphase simulations, extract a bubble shape using the phase indicator $\phi \leq 0$, and approximate the bubble shape by the stair-case line with imposed free-slip boundary condition on it. The obtained bubble velocity is then imposed on the walls. This corresponds to conducting simulations in the reference frame moving with the bubble. Appendix B covers the simple free-slip boundary condition implementation drastically improving velocity patterns. The system is iterated until a steady state is reached. Note, that these type of simulations are much faster than the original multiphase simulations. As the output all the non-zero velocity components perpendicular to the bubble surface are completely eliminated. We compared original multiphase simulations with one-component free-slip simulations. All quantities such as superficial

380 slug and liquid velocities are within 3% for the capillary number in the
 381 range $0.05 \leq Ca \leq 1.0$. One can see in Fig. 7 two streamline profiles
 for $Ca = 0.097$ and $Ca = 1.040$.

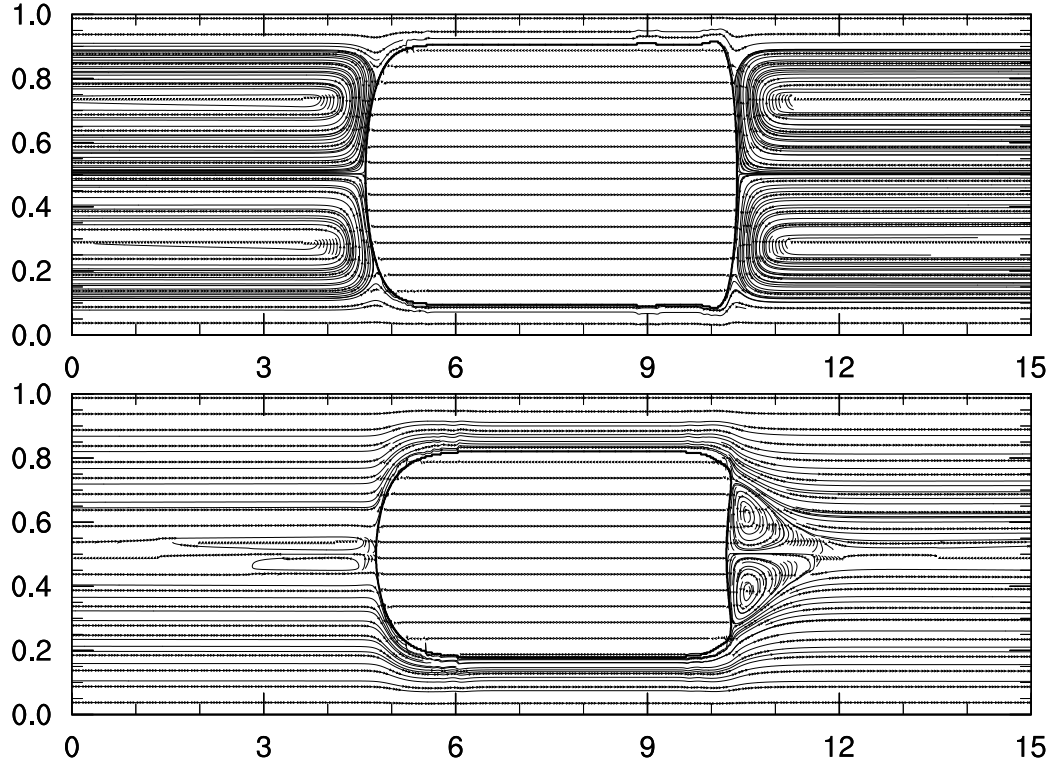


Figure 7: The streamline patterns produced by the free-surface flow solver with simplified approximation of the free-slip bubble surface, see Appendix B. Two completely different velocity patterns are obtained, $Ca = 0.097$ (top) and $Ca = 1.040$ (bottom).

382

383 **Mass transfer** After improved velocity profiles are obtained one can per-
 384 form any mass transfer simulations with the various boundary condi-
 385 tions as covered in Section 2.3. For this purpose one needs to match
 386 the Peclet number Pe taken from experiments.

387 5. Results

388 This section covers simulation results. We first examine the possibility
 389 to increase the fluid velocity while keeping the Peclet number the same.
 390 After that the results for periodic boundary conditions for 5 capillary number
 391 cases will be presented. Finally, we will examine many cell simulations for
 392 two representative velocity patterns related to $Ca = 0.0907$ and $Ca = 1.04$
 393 respectively (see Fig. 7).

394 5.1. Velocity scaling at constant Peclet number

This section addresses the process of significantly increasing the velocity magnitude while keeping dimensionless parameters the same to speed up simulations. This is especially important to be able to simulate a few unit cells in a reasonable time. For example, ten unit cell simulations require a grid of 30000×202 nodes. Since the Peclet number is the only dimensionless quantity governing the advection-diffusion equation:

$$Pe = \frac{U_{\text{bubble}} N_y}{D}. \quad (33)$$

395 one needs to increase the diffusion coefficient when the velocity is increased.
 396 Simulation runs were made with velocities 2, 4, 6, 8, 10, 15, 20, 40 times larger
 397 than the original velocities. The velocities and their corresponding capillary
 398 numbers are presented in Table 2. Periodic boundary conditions were used
 399 and the mass transfer coefficient was calculated according to Eq. 4. Table
 400 2 shows that the velocity limit for periodic boundary conditions is 0.1, so to
 401 be on the safe side, velocities should not be scaled up beyond that value. For
 402 example, in Table 2 for small capillary numbers ($Ca < 0.2$) one can scale up

403 velocity significantly (20 – 40 times) to obtain a velocity around 0.2 where
 404 simulations are still stable. However, for larger capillary numbers the scale
 405 up is smaller (2 – 4 times), and the velocity for stable simulations is smaller
 406 than 0.1 . It gives us a preliminary idea to what extent one can scale periodic
 407 mass transfer simulations. The concentration contour profiles corresponding
 408 to Table 2 for different velocity scalings are presented in Fig. 8. One can
 409 see an acceptable agreement between the cases with the same Peclet number
 410 but different velocity scalings. Note, that the speedup can be up to 10 to 40
 411 times.

412 5.2. Average concentration results

413 In this section we will examine the case where the volume averaged con-
 414 centration over time is used as the characteristic concentration. To calculate
 415 the volumetric mass transfer coefficient we used Eq. 12. Results for the
 416 coefficient $k_L a \frac{U_{\text{bubble}}}{U_{\text{gas}} + U_{\text{liq}}}$ are shown in Fig. 9 for different Peclet numbers and
 417 velocity scalings indicated in Table 2. When the average concentration gets
 418 close to $C^* = 1$ then Eq. 12 gives inadequate results due to accuracy of
 419 the logarithmic function evaluation. This is the reason that curves in Fig.
 420 9 tend to shoot up for long times. Due to velocity scaling each simula-
 421 tion has a different physical time step. Thus, we normalized time such that
 422 it represents a number of unit cell lengths which the bubble will pass, i.e.
 423 $N_{\text{cell units}} = \frac{\text{scale} \cdot U_{\text{bubble}} \cdot N_{\text{iter}}}{L_{\text{unit}}}$. Fig. 9 shows the volumetric mass transfer depen-
 424 dency against the distance in unit cell length. One can see in Table 3 that for
 425 different Peclet numbers different time (number of unit cells) is required to
 426 achieve steady state. For example, for larger Peclet numbers fewer iterations
 427 are required to achieve the steady state condition.

Overall one obtains steady state volumetric mass transfer coefficients for periodic boundaries simulations if the following conditions are fulfilled:

- I** Scaling is performed as $U_{max} = \text{scale} \cdot U_{\text{bubble}} \leq 0.1$.
- II** The larger the Peclet number, the fewer iterations are required. One can extrapolate data from Table 3, say L_{steady} , and estimate the number of iterations to reach the steady-state as $\text{scale} \cdot U_{\text{bubble}} \cdot N_{\text{iter}} \leq L_{\text{steady}}$.

5.3. Periodic boundaries with the inlet/outlet characteristic concentration

The volumetric mass transfer coefficient was calculated using Eq. 12 with the characteristic concentration being the inlet/outlet flux averaged concentration as used by van Baten and Krishna [2]. One can see in Fig. 10 that the calculated volumetric mass transfer behave differently from the domain averaged volumetric mass transfer coefficient. For example, for small capillary numbers, i.e. $Ca = 0.097, 0.254, 0.526$ the values are overpredicted ($k_L a \frac{L_{\text{unit}}}{U_{\text{bubble}} + U_{\text{gas}}} = 0.3, 0.25, 0.1$). When the velocity pattern changes from having a vortex in front of the bubble to not having it, i.e. $Ca = 0.75, 1.04$ the calculated values are underpredicted compared to estimates based on volume-averaged concentration, i.e. $k_L a \frac{L_{\text{unit}}}{U_{\text{bubble}} + U_{\text{gas}}} = 0.06, 0.04$. As we will see later, the domain-averaged characteristic concentration produces proper mass transfer coefficients.

5.4. Van Baten and Krishna formulation

The van Baten and Krishna [2] formulation, Eq. 16, is calculated as the change of mass in the domain divided by the time difference. We examined two approaches: the characteristic concentration taken to be as the domain

average and as the flux-averaged input/output concentration. The latter case corresponds to [2]. The results are presented in Fig. 11 for $Ca = 0.097$ and $Ca = 1.04$. One can see that the inlet/outlet flux averaged concentration is inconsistent. The reason that van Baten and Krishna [2] obtained the mass transfer coefficient close to the analytical estimation is that the liquid slug is well mixed ($Ca < 0.1$ which is below the range studied here) so that the averaged concentration is close to the inlet/outlet concentration.

However, results for the domain-averaged concentration using the approach of van Baten and Krishna are close to simulation results in Section 5.2. Note that for $Ca = 0.097$ the obtained mass transfer coefficient value is 10% lower than the value in Section 5.2. However, as will be shown later the obtained volumetric mass transfer coefficient for $Ca = 0.0097$ has the same value as for the simulations of a few unit cells. Therefore the approach of van Baten and Krishna [2] produces accurate results but if the characteristic concentration is the volume-averaged concentration (not the inlet/outlet flux-averaged concentration used in the original work). From the computational point of view, it also requires the concentration fields in time and space to calculate the mass change in time and the averaged domain characteristic concentration.

5.5. Simulations for several unit cells

In order to achieve independence from the boundary conditions and a closer match with the physical system being modelled, one can simulate several unit cells, corresponding to a head of the bubble train. If end effects are eliminated then the average domain characteristic should change in time according to Eq. 13. This eliminates the ambiguity inherent in choosing a

476 definition of the characteristic concentration, it becomes the same domain-
 477 averaged concentration as the one measured in experiments.

478 This section studies the number of unit cells required for the volumetric
 479 mass transfer coefficient to be independent of the influence of boundaries.
 480 We chose two different velocity patterns (see Fig. 7 for $Ca = 0.097$ and
 481 $Ca = 1.04$) to perform the simulations. For $Ca = 0.097$ we performed
 482 simulations with 4, 6, 8, 10 cells, and for $Ca = 1.040$ only with 4, 6, 8 cells.
 483 We observed however that simulations with a domain length of 10 unit cells
 484 produce the same results as those with 8 unit cells.

485 We keep velocity in the range $0.05 - 0.1$ to avoid excessively long simula-
 486 tion times. The number of steps for mass to pass through the whole domain
 487 can be approximated as $1.5 \frac{L_{\text{unit}}}{U_{\text{bubble}}}$, which takes into account the bulk veloc-
 488 ity. If U_{bubble} is taken as 0.05 then for the domain size $L_{\text{unit}} = 3000$ one can
 489 obtain the following number of iterations for the mass to cross the unit cell
 490 $1.5 \frac{3000}{0.05} = 90000$. Therefore, 10^6 iterations are enough for a system consisting
 491 of 10 unit cells. For more accurate estimations of the number of time steps
 492 depending on the Peclet number we refer to Section 5.1.

493 5.6. $Ca = 0.097$ results

There are two characteristics we want to track in the simulations: the
 average concentration in the unit cell with time (see Eq. 13), and the accu-
 mulated mass rate in the domain which takes into the account inlet/outlet
 fluxes (see Eq. 18). The former resembles experiments: if one has a large
 enough number of unit cells, then the averaged domain concentration should

change in time according to Eq. 13:

$$k_L a \frac{L_{\text{unit}}}{U_{\text{gas}} + U_{\text{liq}}} = \frac{L_{\text{unit}}}{U_{\text{bubble}}(t_2 - t_1)} \ln \left(\frac{C^* - \langle C(t_1) \rangle}{C^* - \langle C(t_2) \rangle} \right) \quad (34)$$

494 The non-dimensional volumetric mass transfer coefficient calculated based on
 495 Eq. 34 (domain-averaged concentration change in time) is represented in Fig.
 496 12 for different unit cells. One can see that mass transfer coefficient values are
 497 the same as the mass flux concentration based on the van Baten and Krishna
 498 formulation with the characteristic concentration being the domain-averaged
 499 concentration (see Section 5.4). This demonstrates two things: the domain-
 500 averaged concentration is the only choice for the characteristic concentration,
 501 and periodic boundary conditions for one unit cell produce good results.

In comparison with periodic boundary conditions Eq. 18 allows to calculate the mass transfer coefficient differently. Eq. 18 can be rewritten as:

$$k_L a \frac{L_{\text{unit}}}{U_{\text{bubble}} + U_{\text{gas}}} = \frac{L_{\text{unit}}}{U_{\text{gas}} + U_{\text{bubble}}} \frac{V \frac{\langle C(t_2) \rangle - \langle C(t_1) \rangle}{t_2 - t_1}}{- \frac{\int C_{\text{outlet}}(L_{\text{unit}}, y, t^*) u(L_{\text{unit}}, y) dy + \int C_{\text{inlet}}(0, y, t^*) u(0, y) dy}{V(C^* - \langle C(t^*) \rangle)}}, \quad (35)$$

502 where t^* is the mean between t_1 and t_2 .

503 Fig. 13 shows average concentrations in different units and $k_L a \frac{L_{\text{unit}}}{U_{\text{bubble}} + U_{\text{gas}}}$
 504 based on Eq. 35 calculated for each unit for velocity scale 10 and 6 unit cells
 505 (all velocity scales produce the same results). It shows that the volumetric
 506 mass transfer coefficient is consistent for internal segments, i.e. unit cells
 507 numbers 2 – 4. The results for the volumetric mass transfer coefficient calculated by Eq. 18 for multiple unit cells are close (less than 10% deviation)
 508 to results for periodic boundary conditions in Section 5.2 . The same dependencies can be found for 8 and 10 unit cells simulations but we do not
 509
 510

511 present them here. We also do not present 4 units cells simulation results
 512 which are highly influenced by entrance and exit effects.

513 The calculation of the volumetric mass transfer coefficient is more difficult
 514 using Eq. 35. However, it will be shown below that this equation can be
 515 significantly simplified in case of larger capillary numbers ($Ca > 0.7$).

516 5.7. $Ca = 1.040$ results

The same correlations were examined for a different velocity pattern at $Ca = 1.040$. The original Peclet number we started with is $Pe = 14041$ (Table 2). To improve stability we changed the original Peclet number by increasing diffusion to $Pe = 2644$. The results with respect to the number of unit cells are the same as for $Ca = 0.097$: at least 6 unit cells are required to avoid the influence of inlet/outlet effects. Thus, only 6 unit cells results are presented in Fig. 14 which shows the average concentration for each unit cell. One can see that the average volume concentration for each unit cell converges to a constant value. Thus, all the mass generated by the bubble is transferred through the boundaries. This indicates that the liquid slug is unmixed since no concentration travels back to inlet with the vortex and increases the average concentration in each unit cell. Note that the periodic boundary conditions cannot show whether the liquid slug is mixed or not due to the fact that the averaged domain concentration always increases in time. Thus, the volumetric mass transfer coefficient $k_L a \frac{L_{\text{unit}}}{U_{\text{bubble}} + U_{\text{gas}}}$ can be calculated according to the definition, Eq. 18:

$$k_L a = \frac{\dot{m} - \int C_{\text{outlet}}(y)u(L_{\text{unit}}, y)dy + \int C_{\text{inlet}}(y)u(L_{\text{unit}}, y)dy}{V(C^* - \langle C(t) \rangle)}, \quad (36)$$

517 where V is the unit cell volume. There is no accumulated mass in the domain,
518 so $\dot{m} = 0$. Like periodic boundary conditions, this case is another extreme
519 limit of Eq. 18. Note that to calculate the volumetric mass transfer coefficient
520 one needs only the spatial information and does not require the knowledge of
521 how the averaged concentration changes in time, which significantly lowers
522 storage requirements for the simulations with $Ca > 0.7$ where there is no
523 vortex in the liquid slug.

524 Fig. 15 (bottom) shows the volumetric mass transfer coefficient based
525 on spatial calculations of inlet/outlet concentrations. One can see that the
526 volumetric mass transfer coefficient is close to the calculated volumetric mass
527 transfer coefficient using the time averaged approach and periodic boundaries
528 one unit cell simulations (presented in the same figure for comparison). Note
529 that results for approaches which incorporate the volume-averaged character-
530 istic concentration either for one cell or a few unit cells coincide. Therefore,
531 for certain hydrodynamic patterns ($Ca > 0.7$), one can easily convert time
532 domain to spatial domain calculations using simulations of several unit cells.

533

534 5.8. *Comparison of experimental and analytical correlations*

While the goal of this paper is not to compare simulation results with
the experimental measurements, we felt that a short note about such com-
parison will be beneficial. Unfortunately, to the authors' knowledge, there
are no reported experimental results measuring the mass flux for bubbles
flowing between parallel plates. However, an interesting correlation for the
mass transfer volumetric coefficient was presented by Yue et al. [7] for three-

dimensional microchannel geometries:

$$k_L a = \frac{2}{d_h} \left(\frac{DU_{\text{bubble}}}{L_{\text{bubble}} + L_{\text{slug}}} \right)^{0.5} \left(\frac{L_{\text{bubble}}}{L_{\text{bubble}} + L_{\text{slug}}} \right)^{0.3}$$

$$k_L a \frac{L_{\text{unit}}}{U_{\text{gas}} + U_{\text{liq}}} = 2 \frac{L_{\text{unit}}}{d_h} \left(\frac{D}{L_{\text{unit}}(U_{\text{bubble}} + U_{\text{gas}})} \frac{U_{\text{bubble}}}{U_{\text{gas}} + U_{\text{liq}}} \right)^{0.5} \left(\frac{L_{\text{bubble}}}{L_{\text{bubble}} + L_{\text{slug}}} \right)^{0.3} \propto Pe^{-\frac{1}{2}} \quad (37)$$

One can see that the volumetric mass transfer correlation should be approximately proportional to $Pe^{-0.5}$. One can also use analytical estimates of the volumetric mass transfer coefficient calculated using the Higbie penetration theory [16]. One can derive the analytical expression for the mass transfer for bubble train flow between parallel plates by following the works [15, 2]:

$$k_L a \frac{L_{\text{unit}}}{U_{\text{bubble}} + U_{\text{gas}}} = \frac{L_{\text{unit}}}{U_{\text{gas}} + U_{\text{liq}}} \left(4 \sqrt{DU_{\text{bubble}}} \pi \frac{\sqrt{L_{\text{bubble}} - H(1 - 2\delta)}}{L_{\text{unit}} H} \right. \\ \left. + 2\sqrt{2} \sqrt{DU_{\text{bubble}}} \frac{\sqrt{H(1 - 2\delta)}}{L_{\text{unit}} H} \right), \quad (38)$$

where H is the channel height, and δ is the non-dimensional film thickness (in channel heights).

Fig. 16 shows a comparison between the correlation by Yue et al. [7], the analytical expression, Eq. 38, and the current simulation results presented in Table 3. The coefficients are close to each other, especially given that the correlation by Yue et al. [7] is for three-dimensional cases. The fitting procedure for this work results showed that the power of the Peclet number dependence is -0.50038 which is close to the theoretical value -0.5 . The fitting curve is $7.745Pe^{-0.50038}$.

6. Summary

This work examines a way to calculate the volumetric mass transfer coefficient of Taylor/Batchelor bubble train flow in the framework of the lattice

Boltzmann method. Overall, the easiest recipe is to perform simulations with
 periodic boundary conditions and calculate the volumetric mass transfer co-
 efficient based on the domain-averaged concentration through any formula-
 tion (van Baten and Krishna, periodic boundary conditions, simulations of
 several unit cells) as they produce consistent results. The best accuracy is
 achieved with formulations based on the mass difference or on the averaged
 domain concentrations taken in different times, Eq. 13. Eq. 11 gives a
 slightly overestimated volumetric mass transfer coefficients (less than 10%).
 The original formulation of van Baten and Krishna [2] is inconsistent if one
 takes the inlet/outlet flux-averaged concentration to be the characteristic
 concentration. Simulations of several unit cells are harder to perform, but
 they indicate how well the liquid slug is mixed. For velocity patterns related
 to $Ca \geq 0.7$ simulations with a few unit cells allow to calculate the volu-
 metric mass transfer coefficient based on the spatial location only, without
 requiring the time snapshots of domain concentration values used in all other
 approaches. Finally, a sample of results was compared with the experimental
 correlation of Yue et al. [7] and shown to be consistent.

7. Acknowledgements

M.J. acknowledges a scholarship from the TWING project co-financed
 by the European Social Fund. A.K. wants to thank Schlumberger for their
 financial support.

568 A. Mass transfer for planar Poiseuille flow

Close to the previous example but with a different velocity profile, the problem can be formulated through the following PDE:

$$\begin{aligned}\frac{\partial C}{\partial x} U(y) &= D \frac{\partial^2 C}{\partial y^2} \\ C(0, y) &= 0, \quad C(x, \pm\delta) = C^*, \quad \frac{\partial C}{\partial y}(x, 0) = 0 \\ U(y) &= U_0 \left(1 - \left(\frac{y}{\delta}\right)^2\right)\end{aligned}\tag{39}$$

The following substitution simplifies the form of equations:

$$\begin{aligned}\zeta &= \frac{x}{\delta} \frac{D}{U_0 \delta} = \frac{1}{Pe} \frac{x}{\delta} \\ \xi &= \frac{y}{\delta}.\end{aligned}\tag{40}$$

Then the following equation can be obtained:

$$\begin{aligned}\frac{\partial \Theta}{\partial \zeta} (1 - \xi^2) &= \frac{\partial^2 \Theta}{\partial \xi^2} \\ \Theta(\zeta, \xi) &= C - C^* \quad \Theta(0, \xi) = -C^* \quad \Theta(0, \pm 1) = 0\end{aligned}\tag{41}$$

After separation of variables, $\Theta(\zeta, \xi) = X(\zeta)Y(\xi)$ one can come up with two equations:

$$\begin{aligned}\frac{dX(\zeta)}{d\zeta} + m^4 X(\zeta) &= 0 \\ \frac{d^2 Y(\xi)}{d\xi^2} + m^4 (1 - \xi^2) Y(\xi) &= 0\end{aligned}\tag{42}$$

The first equation has a solution:

$$X(\zeta) = \exp(-m^4 \zeta)\tag{43}$$

The second equation can be simplified after substitution $\bar{\xi} = m\sqrt{2}\xi$ to the standard equation:

$$Y'' - \left(\frac{1}{4}\bar{\xi}^2 + a\right)Y = 0,\tag{44}$$

where $Y' = dY/d\bar{\xi}$, and $a = -m^2/2$. The equation above has two solutions via parabolic cylinder functions or through the confluent hypergeometric function [46]:

$$\begin{aligned} Y_1 &= e^{-\bar{\xi}^2/4} {}_1F_1\left(\frac{a}{2} + \frac{1}{4}, \frac{1}{2}, \frac{\bar{\xi}^2}{2}\right) \\ Y_2 &= e^{-\bar{\xi}^2/4} {}_1F_1\left(\frac{a}{2} + \frac{3}{4}, \frac{3}{2}, \frac{\bar{\xi}^2}{2}\right) \end{aligned} \quad (45)$$

Taking symmetry conditions into consideration by leaving only the even solution, Eq. 42 has the following solution:

$$Y_m = C_m e^{-m^2 \xi^2/2} {}_1F_1\left(-\frac{m^2}{4} + \frac{1}{4}, \frac{1}{2}, m^2 \xi^2\right) \quad (46)$$

To satisfy the boundary condition we need to find zeros of the hypergeometric function, i.e. ${}_1F_1\left(-\frac{m^2}{4} + \frac{1}{4}, \frac{1}{2}, m^2\right) = 0$. First ten eigenvalues can be found using numerical methods: 1.2967, 2.3811, 3.1093, 3.6969, 4.2032, 4.6548, 5.0662, 5.4467, 5.8023, 6.1373. One needs to satisfy one more condition to obtain coefficients C_m :

$$-C^* = \sum_m C_m e^{-m^2 \xi^2/2} {}_1F_1\left(-\frac{m^2}{4} + \frac{1}{4}, \frac{1}{2}, m^2 \xi^2\right) \quad (47)$$

One can multiply both parts on $(1 - \xi^2) {}_1F_1\left(-\frac{m^2}{4} + \frac{1}{4}, \frac{1}{2}, m^2 \xi^2\right)$ and through orthogonality (Stourm-Liouville theorem) obtain coefficients:

$$C_m = -C^* \frac{\int_{\xi=0}^1 (1 - x^2) e^{-m^2 \xi^2/2} {}_1F_1\left(-\frac{m^2}{4} + \frac{1}{4}, \frac{1}{2}, m^2 \xi^2\right) d\xi}{\int_{\xi=0}^1 (1 - \xi^2) e^{-m^2 \xi^2/2} {}_1F_1\left(-\frac{m^2}{4} + \frac{1}{4}, \frac{1}{2}, m^2 \xi^2\right)^2 d\xi} \quad (48)$$

Therefore the complete solution can be written as:

$$C = C^* - C^* \sum_{m=0} C_m e^{-m^4 \frac{x}{\delta} \frac{1}{Pe}} e^{-m^2 y^2/(2\delta^2)} {}_1F_1\left(-\frac{m^2}{4} + \frac{1}{4}, \frac{1}{2}, m^2 \frac{y^2}{\delta^2}\right), \quad (49)$$

569 where coefficients C_m are taken from Eq. 48. For the case C^* , the first ten
570 coefficients are: 1.2008, -0.2991, 0.1608, -0.1074, 0.0796, -0.0627, 0.0515,
571 -0.0435, 0.0375, -0.0329.

572 B. Free surface boundary conditions

573 There are a few implementations of free boundary conditions [47, 48].
574 However, we developed the easy solver to impose the free surface boundary
575 conditions at the complicated surface of the bubble. The reason is to impose
576 the symmetric boundary conditions. Because the boundary is a staircase
577 approximation, one can find the normal to the boundary which is always
578 located by the angle of multiple of 45 degrees, see Fig. 17. This can be
579 done automatically by the simple coding. Imposing the symmetric boundary
580 conditions requires $U_{n,F}=U_{n,B}$ and $U_{\tau,F} = U_{\tau,B}$. We can copy populations
581 in the certain order to do it, for example $f_{B,i} = f_{F,\bar{i}}$, where c_i and $c_{\bar{i}}$ are
582 complementary directions, where $c_{i,n} = -c_{\bar{i},n}$ and $c_{i,\tau} = c_{\bar{i},\tau}$, where $c_{i,n} =$
583 $(\mathbf{c}_i \cdot \mathbf{n})\mathbf{n}$ and $c_{i,\tau} = \mathbf{c}_i - (\mathbf{c}_i \cdot \mathbf{n})\mathbf{n}$.

584 References

- 585 [1] M.D. Giavedoni and F.A. Saita. The axisymmetric and plane cases of
586 a gas phase steadily displacing a Newtonian liquid - A simultaneous
587 solution of the governing equations. *Phys. Fluids*, 9(8):2420–2428, 1997.
- 588 [2] J.M. van Baten and R. Krishna. CFD simulations of mass transfer from
589 Taylor bubbles rising in circular capillaries. *Chem. Eng. Sci.*, 59:2535–
590 2545, 2004.
- 591 [3] M.T. Kreutzer, F. Kapteijn, J.A. Moulijn, and J.J. Heiszwolf. Multi-
592 phase monolith reactors: Chemical reaction engineering of segmented
593 flow in microchannels. *Chem. Eng. Sci.*, 60:5895–5916, 2005.

- 594 [4] G. Bercic and A. Pintar. The role of gas bubbles and liquid slug lengths
595 on mass transport in the Taylor flow through capillaries. *Chem. Eng.*
596 *Sci.*, 52(21-22):3709–3719, 1997.
- 597 [5] F.P. Bretherton. The motion of long bubbles in tubes. *J Fluid Mech.*,
598 10(2):166–188, 1960.
- 599 [6] G.I. Taylor. Deposition of a viscous fluid on the wall of a tube. *J. Fluid*
600 *Mech.*, 10:161–165, 1961.
- 601 [7] J. Yue, L. Luo, Y. Gonthier, G. Chen, and Q. Yuan. An experimen-
602 tal study of air-water Taylor flow and mass transfer inside square mi-
603 crochannels. *Chem. Eng. Sci.*, 64:3697–3708, 2009.
- 604 [8] R. Gupta, D.F. Fletcher, and B.S. Haynes. Taylor Flow in Microchan-
605 nels: A Review of Experimental and Computational Work. *J. Comput.*
606 *Multiphase Flows*, 2:1–32, 2010.
- 607 [9] M.T. Kreutzer, M.G. van der Eijnded, F. Kapteijn, J.A. Moulijn, and
608 J.J. Heiszwolf. The pressure drop experiment to determine slug lengths
609 in mulitphase monoliths. *Catalysis Today*, 105:667–672, 2005.
- 610 [10] W.B. Kolb and R.L. Cerro. Film Flow in the Space between a Circular
611 Bubble and a Square tube. *J. Coll. Int. Sci.*, 159:302–311, 1993.
- 612 [11] T.C. Thulasidas, M.A. Abraham, and R.L. Cerro. Bubble-train flow in
613 capillaries of circular and square cross section. *Chem. Eng. Sci.*, 50(2):
614 183–199, 1995.

- 615 [12] D. Liu and S. Wang. Hydrodynamics of Taylor flow in noncircular
616 capillaries. *Chem. Eng. and Processing*, 47:2098–2106, 2008.
- 617 [13] A. Kuzmin, M. Januszewski, D. Eskin, F. Mostowfi, and J. Derksen.
618 Three-dimensional binary-liquid lattice boltzmann simulation of mi-
619 crochannels with rectangular cross sections. *Chem. Eng. J.*, 178:306–
620 316, 2011.
- 621 [14] A.L. Hazel and M. Heil. The steady propagation of a semi-infinite bubble
622 into a tube of elliptical or rectangular cross-section. *J. Fluid Mech.*, 470:
623 91–114, 2002.
- 624 [15] S. Irandoust and B. Ertle, S. adn Andersson. Gas-Liquid Mass Transfer
625 in Taylor Flow Through a Capillary. *Canadian J. Chem. Eng.*, 70:115–
626 119, 1992.
- 627 [16] R. Higbie. The rate of absorption of a pure gas into a still liquid during
628 short periods of exposure. *Trans. Amer. Inst. Chem. Eng.*, 31:365–389,
629 1935.
- 630 [17] A. Kuzmin, M. Januszewski, D. Eskin, F. Mostowfi, and J. Derksen.
631 Simulations of gravity-driven flow of binary liquids in microchannels.
632 *Chem. Eng. J.*, 171(2):646–654, 2011.
- 633 [18] U. Frisch, D. d’Humières, B. Hasslacher, P. Lallemand, Y. Pomeau, and
634 J.-P. Rivet. Lattice gas hydrodynamics in two and three dimensions.
635 *Complex Systems*, 1:649–707, 1987.
- 636 [19] G.R. McNamara and G. Zanetti. Use of the Boltzmann Equation to

- 637 Simulate Lattice-Gas Automata. *Phys. Rev. Lett.*, 61(20):2332–2335,
638 1988.
- 639 [20] F.J. Higuera and J. Jimenez. Boltzmann Approach to Lattice Gas Sim-
640 ulations. *Europhys. Lett.*, 9(7):663–668, 1989.
- 641 [21] F.J. Higuera, S. Succi, and R. Benzi. Lattice gas dynamics with en-
642 hanced collisions. *Europhys. Lett.*, 9(4):345–349, 1989.
- 643 [22] D. Yu, R. Mei, L.-S. Luo, and W. Shyy. Viscous flow computations
644 with the method of lattice Boltzmann equation. *Progress in Aerospace
645 Sciences*, 39:329–367, 2003.
- 646 [23] X. Shan and H. Chen. Simulation of nonideal gases and gas-liquid phase
647 transitions by the lattice Boltzmann Equation. *Phys. Rev. E*, 49(4):
648 2941–2948, 1994.
- 649 [24] M.R. Swift, W.R. Osborn, and J.M. Yeomans. Lattice Boltzmann Sim-
650 ulation of Nonideal Fluids. *Phys. Rev. Lett.*, 75(5):831–834, 1995.
- 651 [25] A.K. Gunstensen, D.H. Rothman, S. Zaleski, and G. Zanetti. Lattice
652 Boltzmann model of immiscible fluids. *Phys. Rev. A*, 43(8):4320–4327,
653 1991.
- 654 [26] P. Yuan and L. Schaefer. A Thermal Lattice Boltzmann Two-Phase
655 Flow Model and Its Application to Heat Transfer Problems -Part 2.
656 Integration and Validation. *J. Fluids Eng.*, 128:151–156, 2006.
- 657 [27] R. Zhang and H. Chen. Lattice Boltzmann method for simulations of
658 liquid-vapor thermal flows. *Phys. Rev. E*, 67(066711):1–6, 2003.

- 659 [28] P.J. Dellar. Lattice Kinetic Formulation for Ferrofluids. *J. Stat. Phys.*,
660 121:105–118, 2005.
- 661 [29] G. Falcucci, G. Chiatti, S. Succi, A.A. Mohamad, and A. Kuzmin. Rup-
662 ture of a ferrofluid droplet in external magnetic fields using a single-
663 component lattice Boltzmann model for nonideal fluids. *Phys. Rev. E*,
664 79(056706):1–5, 2009.
- 665 [30] I. Ginzburg. Equilibrium-type and link-type lattice Boltzmann models
666 for generic advection and anisotropic-dispersion equation. *Adv. Wat.*
667 *Res.*, 28:1171–1195, 2005.
- 668 [31] I. Ginzburg. Generic boundary conditions for lattice Boltzmann models
669 and their application to advection and anisotropic dispersion equations.
670 *Adv. Wat. Res.*, 28:1196–1216, 2005.
- 671 [32] I. Ginzburg. Variably saturated flow described with the anisotropic
672 Lattice Boltzmann methods. *Comput. Fluids*, 35:831–848, 2006.
- 673 [33] M. Yoshino and T. Inamuro. Lattice Boltzmann simulations for flow and
674 heat/mass transfer problems in a three-dimensional porous structure.
675 *Int. J. Num. Meth. Fluids*, 43:183–198, 2003.
- 676 [34] J.J. Derksen. Simulations of lateral mixing in cross-channel flow. *Com-*
677 *put. Fluids*, 39:1058–1069, 2010.
- 678 [35] P. L. Bhatnagar, E. P. Gross, and M. Krook. A Model for Collision
679 Processes in Gases. I. Small Amplitude Processes in Charged and Neutral
680 One-Component Systems. *Phys. Rev.*, 94(3):511–525, 1954.

- 681 [36] I. Ginzburg, F. Verhaeghe, and D. d’Humières. Two-relaxation-time
682 Lattice Boltzmann scheme: about parametrization, velocity, pressure
683 and mixed boundary conditions. *Commun. Comput. Phys.*, 3(2):427–
684 478, 2008.
- 685 [37] I. Ginzburg and D. d’Humières. Multireflection boundary conditions for
686 lattice Boltzmann models. *Phys. Rev. E*, 68(066614):1–30, 2003.
- 687 [38] I. Ginzburg. Lattice Boltzmann modeling with discontinuous collision
688 components: Hydrodynamic and Advection-Diffusion Equations. *J.*
689 *Stat. Phys.*, 126(1):157–206, 2007.
- 690 [39] D. d’Humières and I. Ginzburg. Viscosity independent numerical errors
691 for Lattice Boltzmann models: From recurrence equations to ”magic”
692 collision numbers. *Comp. Math. Appl.*, 58(5):823–840, 2009.
- 693 [40] B. Servan-Camas and F. T.-C. Tsai. Lattice Boltzmann method with two
694 relaxation times for advection-diffusion equation: Third order analysis
695 and stability analysis. *Adv. Wat. Res.*, 31:1113–1126, 2008.
- 696 [41] I. Ginzburg. Consistent Lattice Boltzmann schemes for the Brinkman
697 model of porous flow and infinite Chapman-Enskog expansion. *Phys.*
698 *Rev. E*, 77(066704):1–12, 2008.
- 699 [42] I. Ginzburg, D. D’Humières, and A. Kuzmin. Optimal Stability of
700 Advection-Diffusion Lattice Boltzmann Models with Two Relaxation
701 Times for Positive/Negative Equilibrium. *J. Stat. Phys.*, 139(6):1090–
702 1143, 2009.

- 703 [43] A. Kuzmin, I. Ginzburg, and A.A. Mohamad. The role of the kinetic pa-
 704 rameter in the stability of two-relaxation-time advection-diffusion lattice
 705 Boltzmann schemes. *Comp. Math. Appl.*, 61:3417–3442, 2011.
- 706 [44] S. Chapman and T.G. Cowling. *The mathematical theory of non-uniform*
 707 *gases*. Cambridge University Press, Cambridge, third edition, 1995.
- 708 [45] A.D. Polyanin, A.M. Kutepov, A.V. Vyazmin, and D.A. Kazenin. *Hy-*
 709 *drodynamics, Mass and Heat Transfer in Chemical Engineering*. Taylor
 710 and Francis, 2002.
- 711 [46] M. Abramowitz and I. Stegun, editors. *Handbook of mathematical func-*
 712 *tions with formulas, graphs and mathematical tables*. National Bureau
 713 of Standards, 1964.
- 714 [47] I. Ginzburg and K. Steiner. A free-surface lattice Boltzmann method
 715 for modelling the filling of expanding cavities by Bingham fluids. *Phil.*
 716 *Trans. R. Soc. Lond. A*, 360:453–466, 2002.
- 717 [48] X. Yin, D.L. Koch, and R. Verberg. Lattice-Boltzmann method for sim-
 718 ulating spherical bubbles with no tangential stress boundary conditions.
 719 *Phys. Rev. E*, 73:1–13, 2006.

Scale	U_{bubble}	ω_-	Time Itera- tions	C_{aver}
-------	--------------	------------	----------------------	------------

$$Ca = 0.097, Pe = 1313$$

2	0.011	1.98	400000	0.318
4	0.023	1.96	200000	0.319
8	0.044	1.92	100000	0.320
10	0.055	1.90	80000	0.321
20	0.11	1.81	40000	0.324
40	0.22	1.66	20000	0.328

$$Ca = 0.254, Pe = 3414$$

2	0.0286	1.98	800000	0.6533
4	0.0572	1.96	400000	0.6591
8	0.1144	1.92	200000	0.6692
10	0.1430	1.90	160000	0.6734
20	0.2860	1.81	80000	0.6894

$$Ca = 0.526, Pe = 7092$$

2	0.0594	1.98	200000	0.3271
4	0.1188	1.96	100000	0.3315

$$Ca = 0.750, Pe = 10125$$

2	0.0848	1.98	200000	0.3489
---	--------	------	--------	--------

$$Ca = 1.040, Pe = 14041$$

2	0.1176	1.98 ⁴⁹	200000	0.3675
---	--------	--------------------	--------	--------

Table 2: Indications of the achievable stable velocity U_{bubble} when one scales velocity. Since the physical time step represented by a single iteration of the simulation is directly proportional $U_{bubble, LB}$, scaling the velocity directly translates to an effective speed-up of the simulation. Note that time iterations indicated in the table correspond to the same

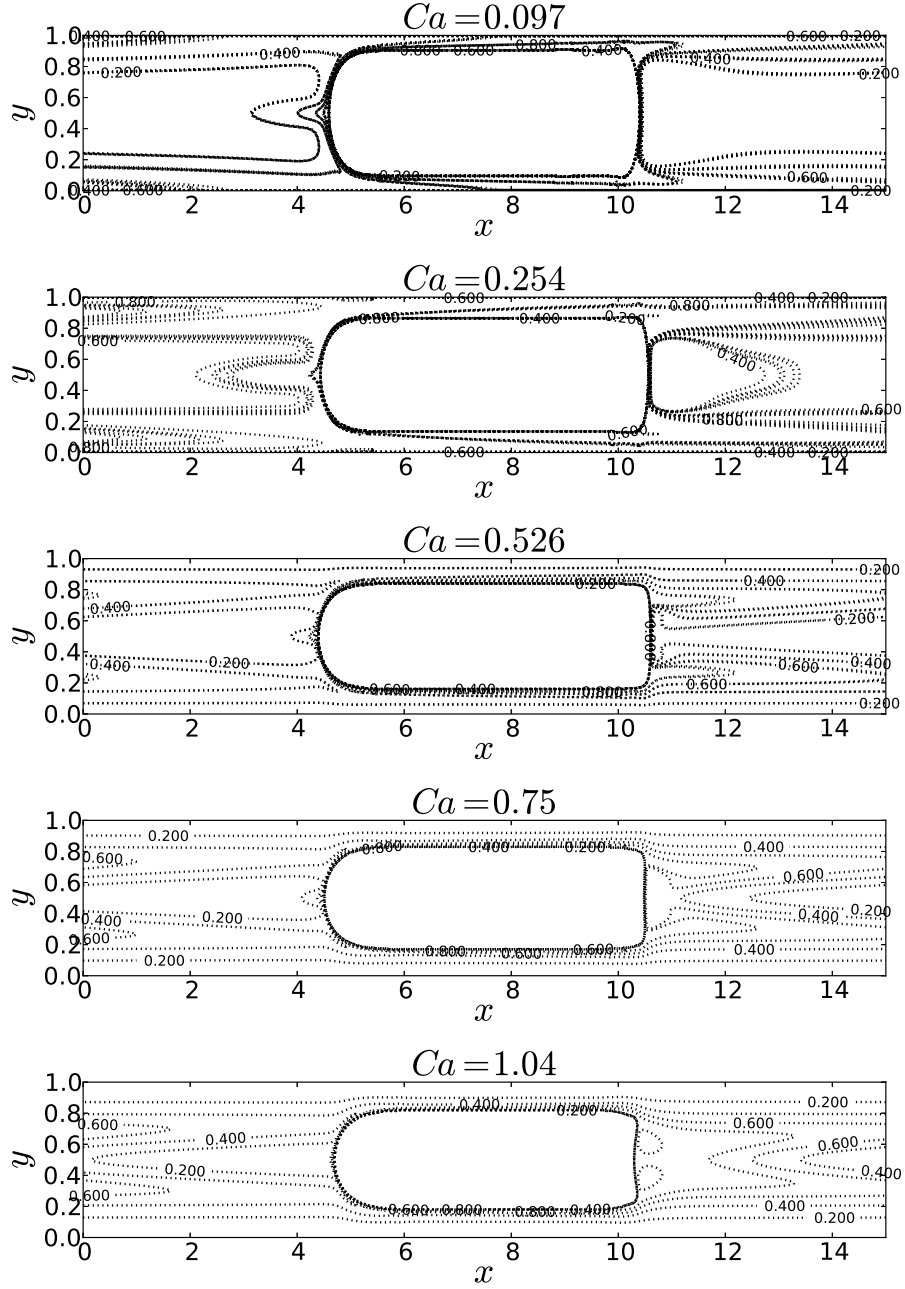


Figure 8: Concentration contour profiles for velocity scalings as identified in Table 2 (top to bottom: $Ca = 0.097, 0.254, 0.526, 0.750, 1.040$). Lines correspond to all different scales indicated in Table 2 (top to bottom: 50 scalings, 5 scalings, 2 scalings, 1 scaling, 1 scaling). Some lines are indistinguishable showing that simulations with velocity scalings are consistent.

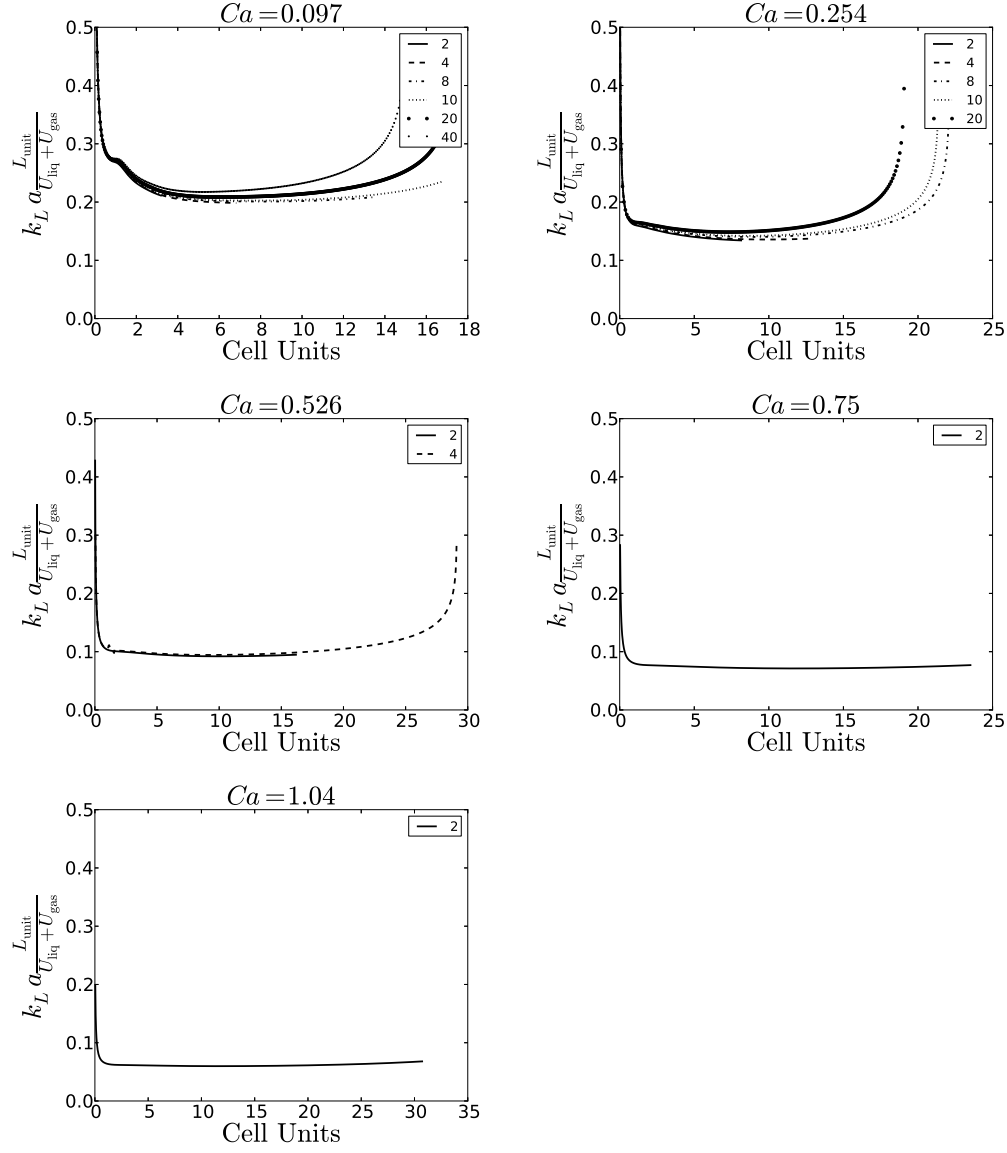


Figure 9: Volumetric mass transfer coefficient for different capillary numbers and scales against the bubble travel distance in the laboratory frame. "Cell Units" axis refers to the physical distance of how many unit cells the bubble travels until the steady state is reached. A legend is provided for velocity scalings. All of them show a good agreement. One can see an abnormal rise of the mass transfer coefficient when the average concentration is close to C^* due to the logarithmic function evaluation. Table 3 summarizes results presented here.

Ca	Pe	$L_{\text{steady}}/L_{\text{unit}}$	$k_L a \frac{L_{\text{unit}}}{U_{\text{bubble}} + U_{\text{gas}}}$
0.097	1313	7	0.21
0.254	3414	6	0.14
0.526	7092	3	0.095
0.750	10125	3	0.074
1.040	14041	2	0.0601

Table 3: The distance which a bubble propagates when the steady-state condition is achieved.

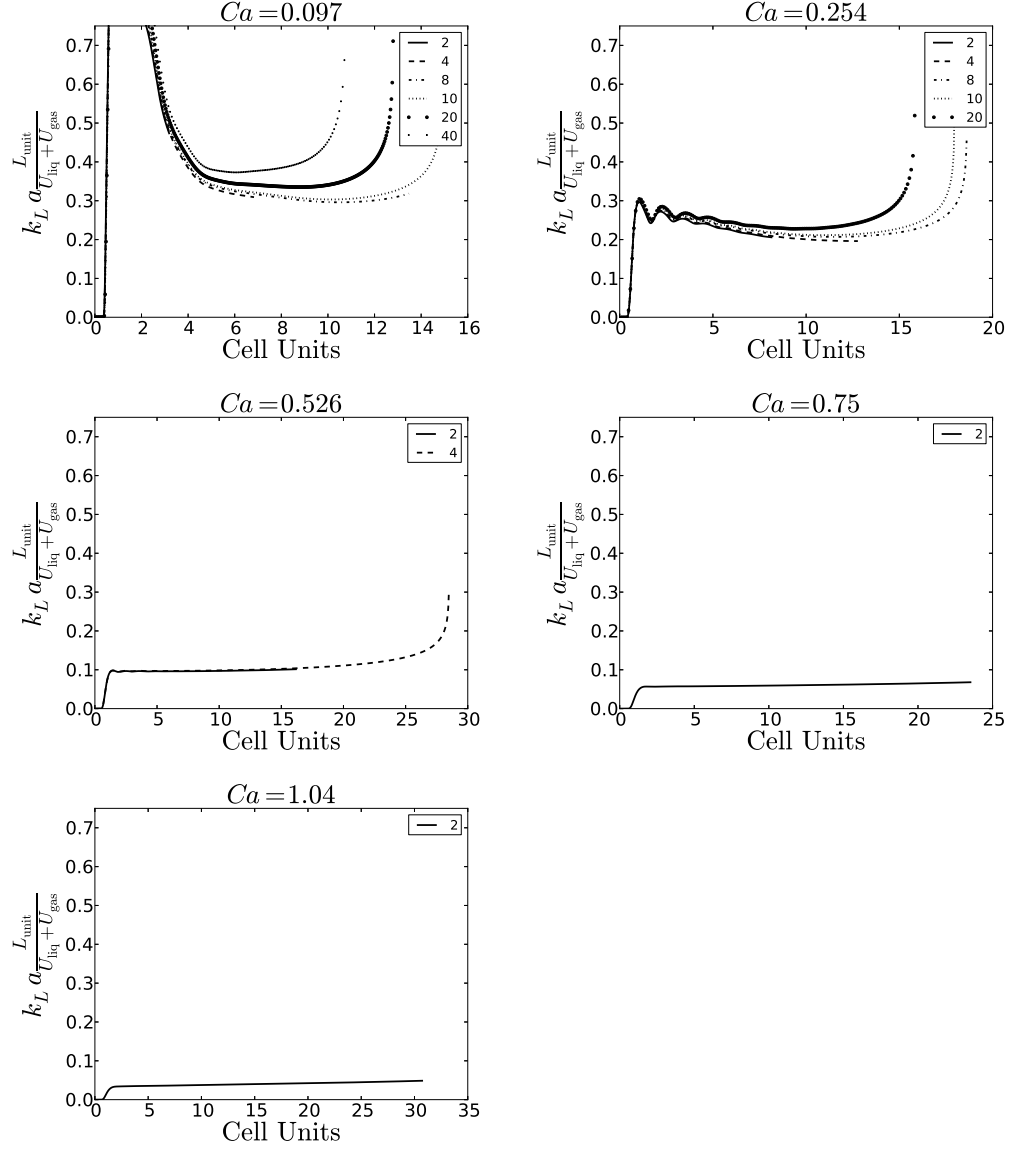


Figure 10: The volumetric mass transfer coefficient with the characteristic concentration based on the inlet/outlet flux averaged concentration as in [2]. One can see that depending on the velocity pattern, the values are either overpredicted or underpredicted in comparison to values specified in Table 3

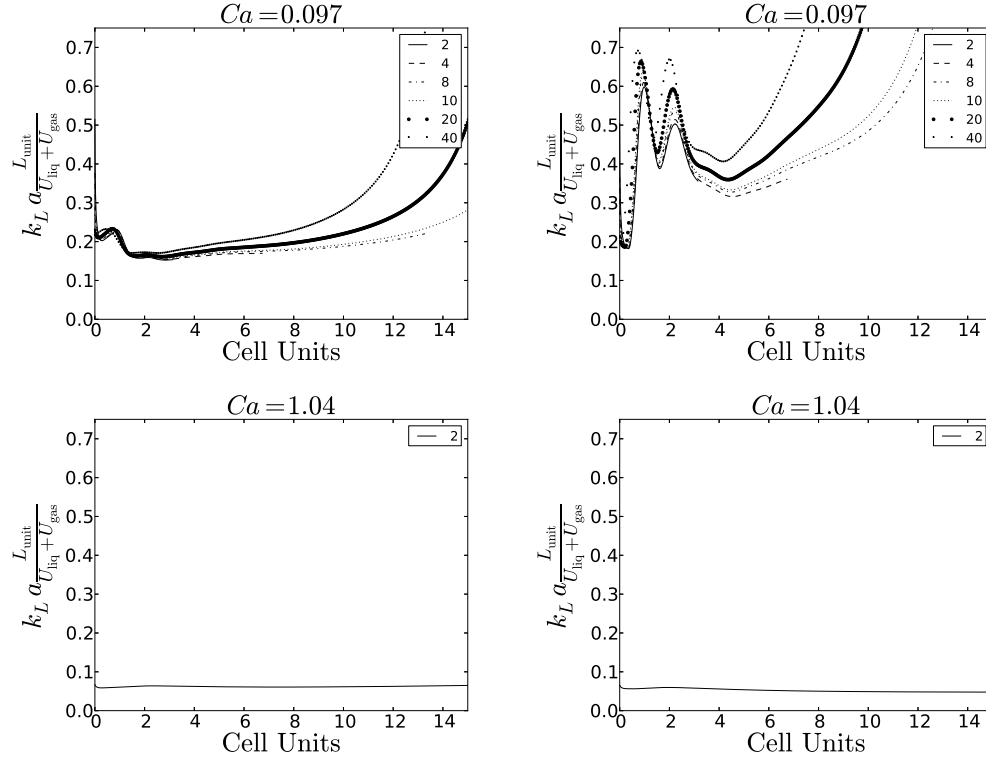


Figure 11: The van Baten and Krishna [2] formulations for $Ca = 0.097$ (top) and $Ca = 1.04$ (bottom) with the characteristic concentration being domain-averaged (left) and inlet/outlet flux-averaged (right). One can see that the van Baten and Krishna [2] formulation produces good results with the characteristic concentration being the average concentration. Moreover, the values are closer to values obtained with many cell simulations, see Fig. 12, than in comparison with periodic boundary simulations in Section 5.2. However, the characteristic concentration being inlet/outlet flux-averaged does not produce consistent results.

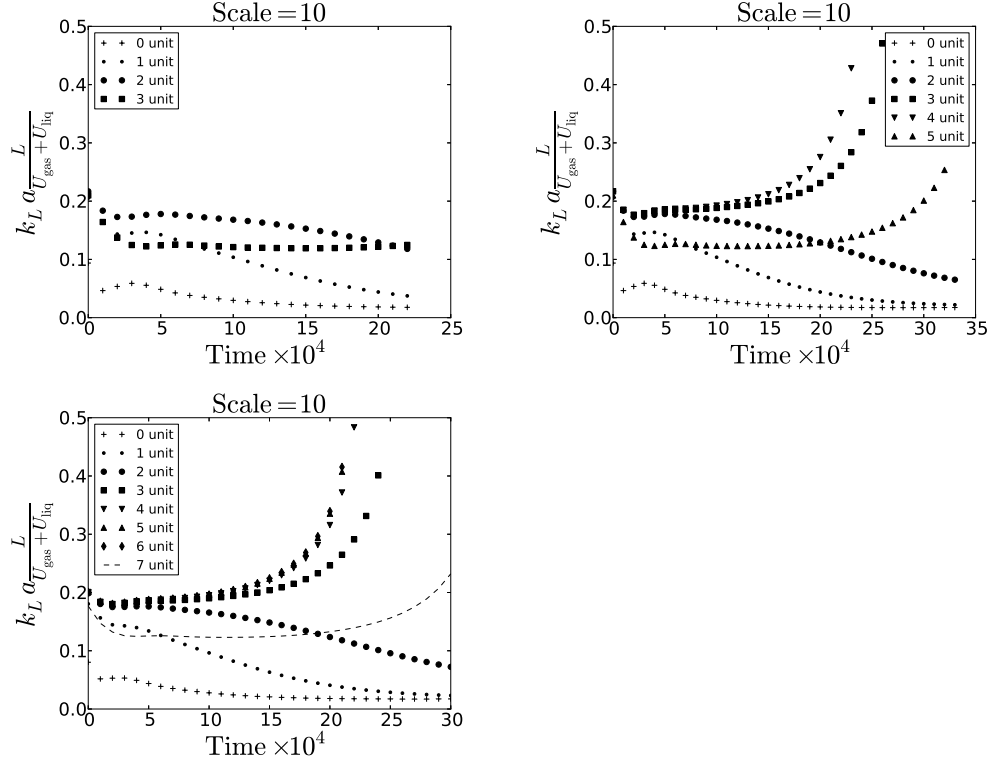


Figure 12: The non-dimensional volumetric mass transfer coefficient defined in Eq. 34 for 4 (top left), 6 (top right), 8 unit cells (bottom). Only scale 10 is presented since all other simulations produce the same results. One can see that 4 unit cells is not enough to avoid the influence of boundaries. However, the results for 6 and 8 unit cells are consistent and show that beginning from third unit cell the results and ending with the penultimate cell results are consistent with periodic boundary simulations and van Baten and Krishna [2] formulations.

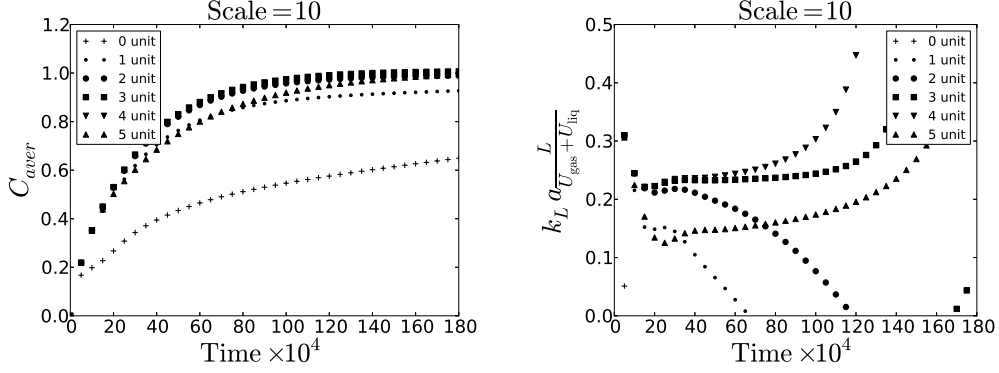


Figure 13: Average concentrations (left) and volumetric coefficients (right) for 6 unit cells. The volumetric mass transfer coefficient is calculated based on Eq. 35 and accounts for inlet and outlet fluxes.

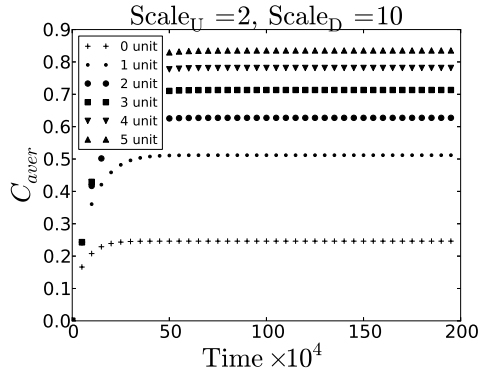


Figure 14: Results for 6 unit cells. The Peclet number equals to $Pe = 2644$. One can see that average concentrations reach certain value and stay constant. Thus, the volumetric mass transfer coefficient, $k_L a \frac{L_{unit}}{U_{bubble} + U_{gas}}$, can be calculated using the spatial approach, see Fig. 15.

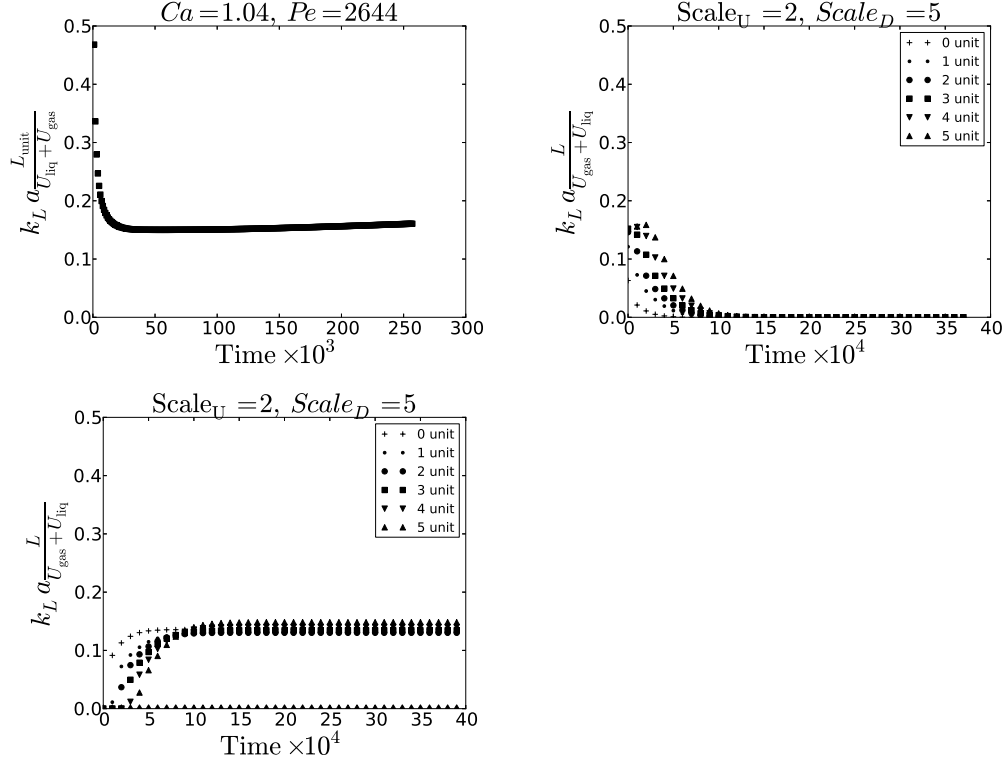


Figure 15: The periodic (top left, 1 unit cell, Eq. 13), unit cells domain-averaged concentrations as a function of time (top right, 6 unit cells, Eq. 13), and spatial location (bottom, 6 unit cells, Eq. 36) calculated volumetric mass transfer coefficients. One can see that they all coincide. However, the calculations based on periodic boundary conditions produce a slightly overestimated volumetric mass transfer coefficient. One can as well see that the domain-averaged concentration simulations (top right) reach the steady volumetric concentration fast and start decaying after that. It is not convenient to use them in practical cases for unmixed slug, i.e. $Ca > 0.7$.

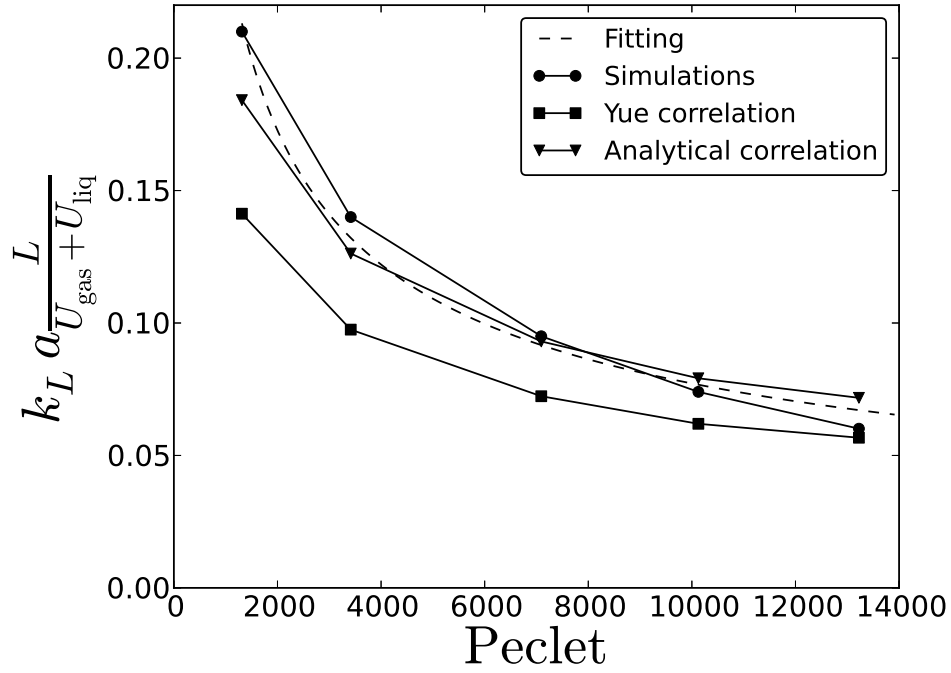


Figure 16: Comparison between the correlation by Yue et al. [7], the analytical correlation derived by following the work [15] and the mass transfer coefficient based on periodic boundary conditions. The fitting curve ($7.745Pe^{-0.50038}$) is proportional to $Pe^{-0.5}$ which corresponds to all correlations. One can as well see that the deviation from the analytical expression becomes larger with the increasing Peclet number, which happens because the analytical expression does not account for the velocity pattern and the bubble shape change.

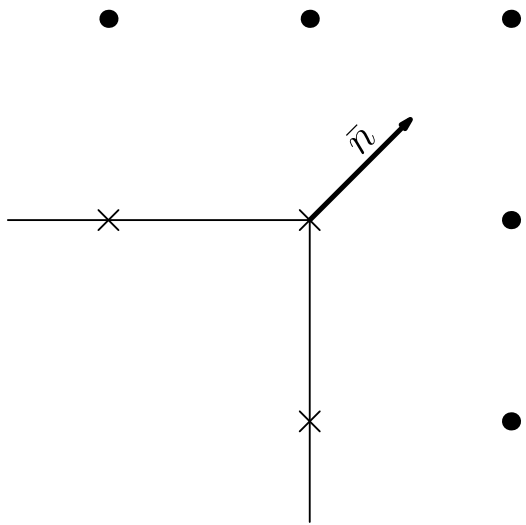


Figure 17: Free-surface boundary condition represented in the lattice Boltzmann method. Boundary nodes are depicted by crosses, and fluid nodes are represented by dots. The populations at the corner boundary nodes are essentially the populations of the fluid node, but in a different order.